Neutron Stars and NuSTAR

A Systematic Survey of Neutron Star Masses in High Mass X-ray Binaries

&

Characterization of CdZnTe Detectors for NuSTAR

A Thesis by
Varun B. Bhalerao
Advisors
Professors Fiona Harrison & Shri R. Kulkarni

In Partial Fulfillment of the Requirements
for the Degree of
Doctor of Philosophy

California Institute of Technology
Pasadena, California

2012

(Defended May 24, 2012)

Dedicated to my parents,
Erawati and Bhalchandra Bhalerao
my role models, motivation,
and strength.

Acknowledgments

My six years at Caltech have been an amazing experience, in both work and personal life. As I write this thesis summarizing the work, it is fitting that I begin by thanking the many people who have made my little achievement possible.

I am very fortunate to have Professors Fiona Harrison and Shri Kulkarni as my advisors. Their foresight, work ethic, and complementary styles of mentoring provided all the ingredients necessary to take me through my thesis. They have provided all resources I needed, and key insights whenever I was short on ideas (or had too many). I have learned a lot from working with them, and will continue striving to live up to their standards.

Working on NuSTAR has been a dream come true. No, really. Who has not wanted to build and launch a satellite? My work would have been impossible without significant help from my lab partners Brian Grefenstette and Vikram Rana. As the junior-most member in the Caltech NuSTAR team, I was the least experienced. I am grateful to Eric Bellm, Jill Burnham, Rick Cook, Takao Kitaguchi, Kristin Madsen, Peter Mao, and Hiromasa Miyasaka for helping me whenever I was stuck. I thank Peter's dentist. Miles Robinson, Steve Stryker, and Robert Crabill have been wonderful troubleshooters and the go-to people for any work in the laboratory. Summer projects by students Nancy Wu and Suk Sien Tie laid good foundations for my future work.

As an electrical engineer, I had a lot to learn about astronomy. My foray into observations was possible thanks to the enthusiastic guidance of Mansi Kasliwal. I thank Professor Marten van Kerkwijk for teaching me how to extract every last bit of information from data—a skill I still strive to perfect. Brad Cenko was extremely helpful in my first year photometer project. I thank Mike Muno for his early work on radial velocities of high mass X-ray binaries, which developed into my observational project. My batchmates Laura, Walter, Matthew, and Yacine have been a constant source of support and inspiration at

Caltech. My work would have been nowhere as much fun without my long-time officemates Gwen and Laura. Together with Mansi, Shriharsh, Swarnima, and Abhilash, they made work a lot of fun! Shriharsh was the sounding board for new ideas at work. I am glad to have the company of Swarnima, Ryan and Krzysztof to share my passion of outreach and amateur astronomy.

Part of what makes Caltech special is the excellent administrative and technical staff, whose success lies in the fact that they are always in the background. My first-year project and subsequent observing runs and Palomar were a pleasure thanks to Kevin Rykoski, Dipali, and Jean Mueller. I thank Richard Dekany, Dan McKenna, and Jeff Zolkower for support on my first year project. The ADPF group, especially Partrick Shopbell and Anu Mahabal, have maintained an excellent computing infrastructure—giving me freedom from install logs and core dumps. Librarians Lindsay Cleary and Joy Painter always went out of their way to help with procuring and issuing books. Special thanks to the several administrative assistants at Caltech: Debby Miles, Nina Borg, and Caprece Anderson at the Space Radiation Laboratory, Bronagh Glaser at Geology and Planetary Sciences, Gina Armas and Gita Patel in Robinson and Cahill, and Teresita Legaspi at the Registrar's Office. Their untiring efforts ensured that I could focus on my work without ever being bogged down by paperwork.

The reason I can put my work at the forefront is an extremely supportive family. None of this would have been possible without the effort and encouragement of my parents, who have placed me and my career ahead of everything else. Sneha has been my motivation through this final phase of my Ph.D.. My extended family, Shri and Shaila Mate, Prasanna, Madhuri, and Amruta Mate have always been around for me. Games with the badminton group at Caltech were a constant source of refreshment (and exercise!). And finally, my family away from home: Mansi, Prabha, Pinkesh, Jayakrishnan, Sushree, Shriharsh, and Ishwari, who have done everything possible to keep me happy. Thank you. *You're awesome*!

Abstract

My thesis centers around the study of neutron stars, especially those in massive binary systems. To this end, it has two distinct components: the observational study of neutron stars in massive binaries with a goal of measuring neutron star masses and participation in NuSTAR, the first imaging hard X-ray mission, one that is extremely well suited to the study of massive binaries and compact objects in our Galaxy.

The Nuclear Spectroscopic Telescope Array (NuSTAR) is a NASA Small Explorer mission that will carry the first focusing high energy X-ray telescope to orbit. NuSTAR has an order-of-magnitude better angular resolution and has two orders of magnitude higher sensitivity than any currently orbiting hard X-ray telescope. I worked to develop, calibrate, and test `CdZnTe` detectors for NuSTAR. I describe the `CdZnTe` detectors in comprehensive detail here—from readout procedures to data analysis. Detailed calibration of detectors is necessary for analyzing astrophysical source data obtained by the NuSTAR. I discuss the design and implementation of an automated setup for calibrating flight detectors, followed by calibration procedures and results.

Neutron stars are an excellent probe of fundamental physics. The maximum mass of a neutron star can put stringent constraints on the equation of state of matter at extreme pressures and densities. From an astrophysical perspective, there are several open questions in our understanding of neutron stars. What are the birth masses of neutron stars? How do they change in binary evolution? Are there multiple mechanisms for the formation of neutron stars? Measuring masses of neutron stars helps answer these questions. Neutron stars in high-mass X-ray binaries have masses close to their birth mass, providing an opportunity to disentangle the role of "nature" and "nurture" in the observed mass distributions. In 2006, masses had been measured for only six such objects, but this small sample showed the greatest diversity in masses among all classes of neutron star binaries. Intrigued by

this diversity—which points to diverse birth masses—we undertook a systematic survey to measure the masses of neutron stars in nine high-mass X-ray binaries. In this thesis, I present results from this ongoing project.

While neutron stars formed the primary focus of my work, I also explored other topics in compact objects. appendix A describes the discovery and complete characterization of a 1RXS J173006.4+033813, a polar cataclysmic variable. appendix B describes the discovery of a diamond planet orbiting a millisecond pulsar, and our search for its optical counterpart.

Contents

List of Figures

List of Tables

List of Acronyms

ADC: analog-to-digital convertor

AGN: active galactic nuclei

ASIC: application-specific integrated circuit

BH: black hole

cps: counts per second

DBSP: double beam spectrograph

EOS: equation of state

ESD: electrostatic discharge

FITS: flexible image transport system

FOV: field of view

FPGA: field programmable gate array

FPM: focal plane module

FWHM: Full Width at Half Maximum

GUI: graphical user interface

HEASARC: high energy astrophysics science archive research center

HMXB: high-mass X-ray binary

HPD: half power diameter

HV: high voltage

IC: integrated circuit

IR: infrared

LRIS: low resolution imaging spectrograph

MISC: minimum instruction set computer

MOC: mission operations center

NRL: naval research laboratory

NS: neutron star

NuSTAR nuclear spectroscopic telescope array

NuSTARDAS: NuSTAR data analysis software

OGIP: office of guest investigator programs

PH: pulse height

PI: pulse invariant

PMT: photomultiplier tube

PSF: point-spread function

RMF: redistribution matrix file

QE: quantum efficiency

RV: radial velocity

SAA: south atlantic anamoly

SFXT: supergiant fast X-ray transient

SMBH: super massive black hole

SMEX: small explorer

SNR: signal-to-noise ratio

SOC: science operations center

SRL: space radiation laboratory

ToO: target of opportunity

XRB: X-ray binary

Part One: NuSTAR

Characterization of CdZnTe Detectors for NuSTAR

Image: NuSTAR satellite at Orbital Sciences Corporation

Chapter 1

NuSTAR: The Nuclear Spectroscopic Telescope Array

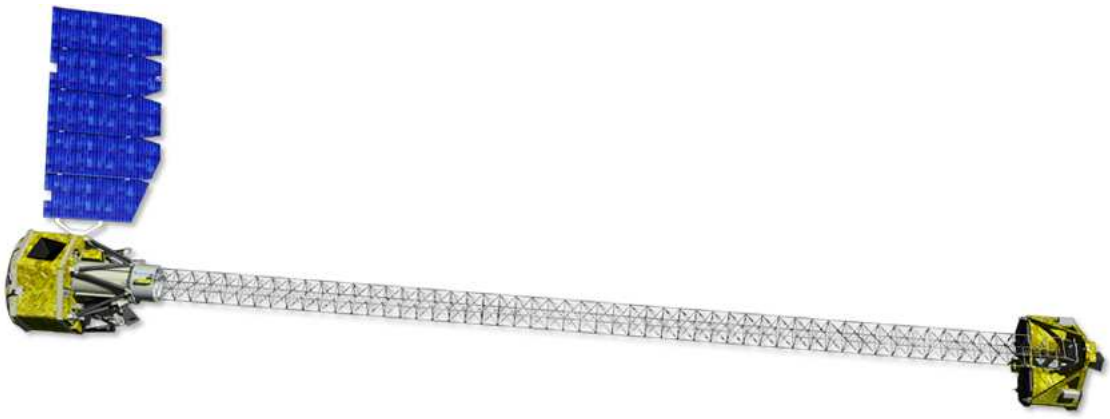

1.1 Hard X-rays

As the universe evolves around us, astronomers examine it from a single vantage point to piece together its working. The pieces of this jigsaw puzzle are information obtained from various wavelengths. Evolving well beyond the old optical telescopes, observational astrophysics now assimilates information from the entire electromagnetic spectrum: extending from the low energy radio waves to high energy gamma rays, spanning over 10 orders of magnitude in energy. Astrophysics also incorporates information from non-electromagnetic channels like cosmic rays, neutrinos and eventually will directly utilize gravitational waves. Harwit (2003) makes an excellent case that technological breakthroughs have ushered in major advances in our knowledge of the cosmos: sometimes by opening up a new energy

range for study, at other times by greatly increasing the sensitivity in an energy range.

A relatively underexplored part of the electromagnetic spectrum is the hard X-ray band. X-rays are high energy photons, with energies from few hundred electron volts (eV) to several hundred kilo electron volts (keV) (figure 1.1). This interval is loosely divided into soft X-rays and hard X-rays. Here, we will refer to the energy range covered by NuSTAR (6 to 80 keV) as the Hard X-ray band.

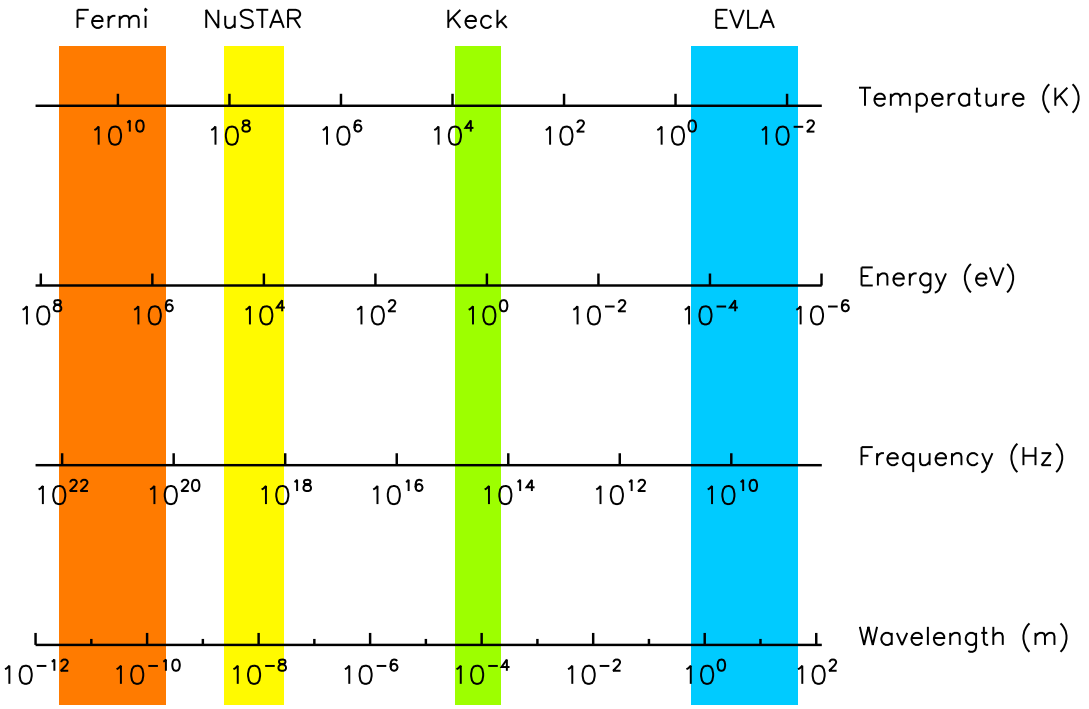

Figure 1.1. The electromagnetic spectrum. The four axes from bottom to top show the wavelength (m), frequency (Hz), energy (eV), and a characteristic temperature (K) for radiation ranging from high energy gamma rays on the left to radio waves on the right. Shaded areas represent energy ranges for a few telescopes. NuSTAR will probe the hard X-ray band from 6 keV to 80 keV (0.15 – 2 Å).

Extending sensitivity to high energy X-rays enables studies of nonthermal processes, often masked at lower energies by thermal plasma emission. For example, synchrotron radiation from hot ionized gas in galaxy clusters is detected in radio wavelengths. However, neither the magnetic field strength nor the number density of electrons can be independently calculated from these data (Rephaeli et al., 2008). The same electrons responsible

for the synchrotron radiation will Compton upscatter cosmic microwave background (CMB) photons into the X-ray band. In the soft X-ray band, this radiation is dwarfed by thermal emission from the cluster. Hard X-ray observations are the key to detecting and characterizing the nonthermal emission to further our understanding of the intracluster medium (ICM).

Enhanced sensitivity at higher energies also opens unique opportunities to study emission from radioactive decay. For example, both core collapse and thermonuclear supernovae produce radioactive $^{44}\mathtt{Ti}$, which emits nuclear deexcitation lines at 68 and 78 keV during radioactive decay. Theoretical predictions for $^{44}\mathtt{Ti}$ production in both types supernovae are widely scattered, and are sensitive to the turbulence and asymmetry in the explosion. For core collapse supernovae, the amount of $^{44}\mathtt{Ti}$ produced depends on the location of the mass cut: the boundary ejecta and material that falls back. The total luminosity in these lines provides a direct measure of the amount of $^{44}\mathtt{Ti}$ produced, thus constraining the explosion physics.

Hard X-ray radiation is highly penetrating. Some sources, e.g., Compton thick AGN, are enshrouded in dust and gas, which absorb and reprocess most of the source radiation. As the absorption cross section for X-rays in material of typical abundances decreases sharply with energy, these sources can still be studied in hard X-rays.

Sensitive hard X-ray telescopes can provide valuable insights into the physics of these and many other astrophysical sources. I discuss current hard X-ray telescopes in Section 1.2, followed by an overview of a next-generation hard X-ray telescope, NuSTAR (Section 1.3).

1.2 Hard X-ray Telescopes

As the Earth's atmosphere is opaque to X-rays, developments in X-ray astronomy lagged significantly behind those in optical or radio astronomy. In 1948, a set of detectors on board a V2 rocket detected X-rays from the Sun—the first detection of non–terrestrial X-rays (Tousey et al., 1951). It took well over a decade for the detection of a cosmic point source: a feat accomplished by Giacconi et al. (1962) by the discovery of Sco X-1. Ever since, the history of X-ray astronomy has been marked by technological breakthroughs going

hand-in-hand with astronomical motivation to make better and better satellites,[1,2] which are many orders of magnitude more sensitive than these pioneering experiments (Table 1.1).

These developments in technology warrant a bit more attention to place NuSTAR in context. The most basic elements of an X-ray telescope are the light gathering aperture and the detectors. Early X-ray experiments had very little directionality. Solar X-rays were first discovered by a crude pinhole camera payload on board a Naval Research Laboratory rocket, with no means to collimate or focus the incoming radiation. The next evolutionary step was to add collimators in front of the detectors. Collimators enable basic imaging of the sky in the same way a single dish radio telescope does: by pointing and imaging one field of view at a time. They are still used primarily for X-ray timing, for example in the Proportional Counter Array on board the Rossi X-ray Timing Explorer (RXTE; Jahoda et al., 1996). Finer imaging is achieved by using coded aperture masks—which uses the principle of pinhole cameras. The aperture consists of a mask with a non–repeating pattern of holes, placed some distance away from a detector (Figure 1.2). The location of a point source in the sky can be inferred from the shadow it casts. The sky image is reconstructed by deconvolving the observed image with the pattern of holes in the aperture. As in pinhole cameras, the angular resolution is governed by the size of holes in the mask and the mask-to-detector distance. Coded aperture masks have a wide field of view, making them the preferred instruments for monitoring transients. Current coded aperture mask instruments include the Burst Alert Telescope (BAT; Barthelmy et al., 2005) on *Swift* as well as IBIS (Imager on Board the *Integral* Spacecraft) and ISGRI (the *Integral* Soft Gamma-Ray Imager) on *Integral* (Ubertini et al., 2003; Lebrun et al., 2003).

A major breakthrough in soft X-ray astronomy came with the development of focusing optics. Unlike visible light, X-rays do not reflect near normal incidence. The index of refraction of solids for X-rays is slightly lower than unity. Hence, if X-rays are incident on a surface at incidence (or graze angles) below the critical angle, they undergo total external reflection. Based on this principle, the Einstein Observatory (HEAO 2; Giacconi et al., 1979) became the first satellite to use focusing X-ray optics. Today, focusing optics are regularly employed in soft X-ray telescopes. Most notable among them is *Chandra*, which attains subarcsecond angular resolution (Weisskopf et al., 2000).

[1] https://en.wikipedia.org/wiki/History_of_X-ray_astronomy

[2] http://heasarc.gsfc.nasa.gov/docs/heasarc/headates/heahistory.html

Table 1.1. Currently operating X-ray telescopes compared to NuSTAR

Telescope / Instrument	Detector type	Energy range (keV)	Energy resolution (keV)[a]	Optics type	Effective area (cm^2)	Angular resolution (FWHM)	Field of view	Launch
Chandra ACIS	CCD	0.1–10	0.13	Focusing	235	$1''$	$17'$	1999
XMM-Newton EPIC PN	CCD	0.2–12	0.13	Focusing	851	$\sim 6''$	$30'$	1999
Suzaku XIS	CCD	0.2–12	0.12	Focusing	1000	$< 1.5'$	$19'$	2005
Suzaku HXD	PIN diodes	10–60	3	Collimators	140	$34'$	$34'$	2005
Integral IBIS/ISGRI	CdTe	15–1000	9% (100 keV)	Coded Aperture	~ 2600 cm^2	$12'$	$19°$ [b]	2002
Swift BAT	CZT	15–150	7	Coded Aperture	5240	$17'$	1.4 sr [c]	2002
NuSTAR	CZT	6–80	1	Focusing	920	$10''$	$13'$	2012

Note. — Data sources: Suzaku PIN: Takahashi et al. (2007), *Integral*: Ubertini et al. (2003), Swift: Barthelmy et al. (2005), NuSTAR: Harrison et al. (2010), all others from http://heasarc.nasa.gov/docs/heasarc/missions/comparison.html, retrieved on 2012 March 12. Other relevant high energy telescopes not mentioned here include HETE-2, MAXI, AGILE, Fermi and the upcoming HXMT, SRG (with ART-XC), Astro-H, *AstroSat* and GEMS.

[a]Energy resolution at 6 keV for soft X-ray instruments and 60 keV for hard X-ray instruments.

[b]Partially coded FOV. Fully coded field is 9°.

[c]Half coded field. 1.4 sr = 4600 sq. deg.

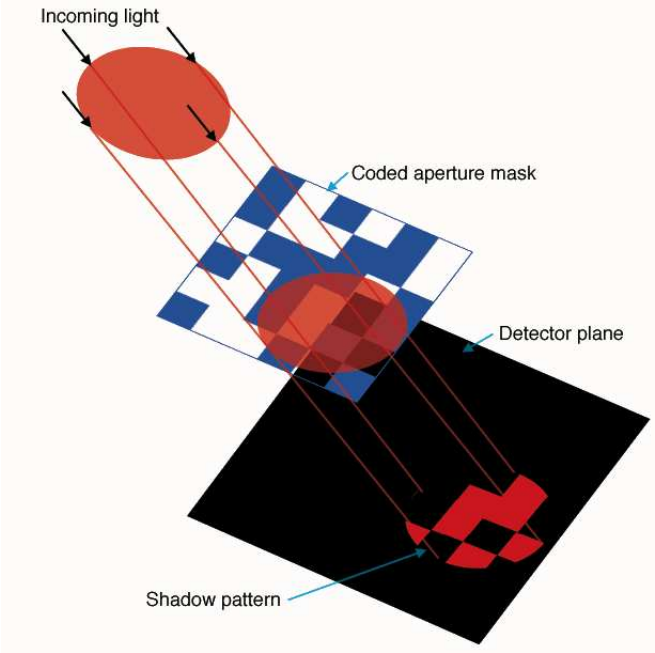

Figure 1.2. Imaging with a coded aperture mask. When light from astrophysical sources (red) is incident on the coded aperture mask (blue), it casts a particular shadow on the detector plane (black). The shape of the shadow and its location on the detector uniquely determine the location of the source in the sky. If the source extent is greater than the angle subtended by an individual mask "pixel" on the detector, then source morphology can be inferred from the image as well.
Image from http://swift.sonoma.edu/about_swift/instruments/bat.html.

Focusing telescopes concentrate light from the source onto a detector much smaller than the telescope aperture. Since sources can be extracted from smaller parts of the detector, the contributions from astrophysical and detector backgrounds are greatly reduced relative to a coded aperture mask. For example, NuSTAR has a collecting area of $\sim$ 400 cm^2 at 20 keV. Hard X-rays from a point source are focused into a few square-millimeter spot. As compared to a coded aperture mask where the detector area is about a factor of two larger than the aperture, this reduces the background in the extraction region by 10^4 and improves the SNR by a factor of 100 in background–limited observations. Compared to coded aperture masks, focusing telescopes are also more sensitive to diffuse sources.

In spite of the advantages they offer, several technical challenges have prevented adaption of focusing optics to hard X-ray. The critical angle below which X-rays undergo total

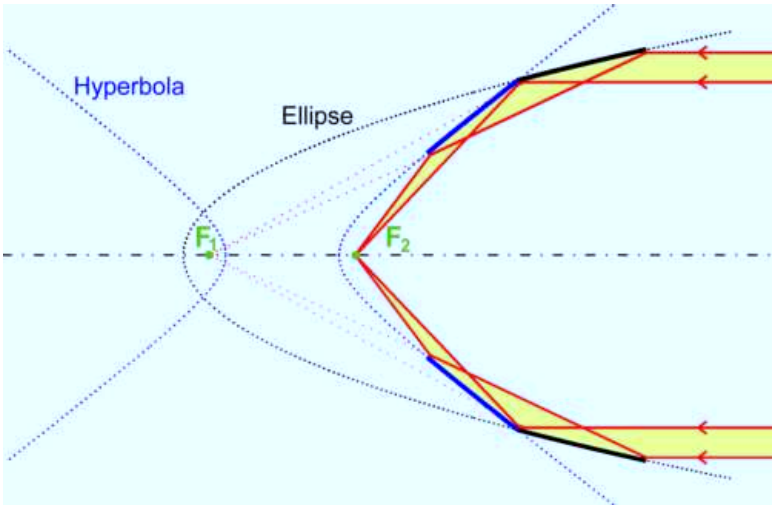

Figure 1.3. A sketch of Wolter-I focusing optics (Wolter, 1952a,b). X-rays incident from the right side are first reflected toward the focus F_1 by a parabolic surface, shown in solid black. These rays undergo a second reflection from a hyperbolic surface (shown in solid blue) to converge at the focus F_2. The two-mirror arrangement reduces the total focal length by roughly a factor of two, and improves image quality across the entire field of view. Image reproduced with permission from http://www.x-ray-optics.de, retrieved 2012 March 07.

external reflection varies approximately linearly with wavelength. Hence, for a given focal length, the maximum aperture area of a hard X-ray telescope working at 10 keV that relies only on critical angle reflection is approximately one-hundredth that of a soft X-ray telescope working at 1 keV.

One way to overcome the critical angle limitation is to use multilayer coatings (Christensen et al., 1992; Madsen et al., 2009; Christensen et al., 2011). A multilayer is a stack of thin, alternating layers of two different materials. Multilayers extend reflectivity beyond the critical angle using Bragg reflection. Because partial reflection happens at interfaces between materials of different index of refraction, the stack acts as a periodic lattice, enhancing reflectivity by constructive interference where the Bragg condition is satisfied: $2d \sin\theta = m\lambda$. Here, d is the bilayer thickness, θ is the angle of incidence, λ is the wavelength of the incident photon, and m is the order of reflection. A fixed-thickness multilayer design will lead to enhanced reflectivity at fixed energies where the Bragg condition is satisfied. Broadband reflectivity can be enhanced by using depth-graded multilayers, where a varying thickness

in the d-spacing as a function of depth in the coating shifts the Bragg peaks through the spectrum. The reflectance at an interface is proportional to the density (or refractive index) contrast between the two materials. Hence, multilayers are composed of a high density (high refractive index) and a low density material, like tungsten and silicon. The effect of the multilayers is to increase the reflectance angle above the critical angle, with reflectance depending on the minimum d-spacing and design of the layers (Mao et al., 1999). Even with multilayers, extending reflectivity to high energies required telescopes with graze angles smaller than utilized in soft X-rays. For a single surface, the ratio of mirror surface area to the projected collecting area is very low. Collecting area is increased by nesting multiple optics with the same focal point. Hence, many mirrors with large surface area need to be coated with multilayers and aligned within strict tolerances: a technically challenging procedure. Developing depth graded multilayer coated optics was a key item enabling the NuSTAR telescope.

Of equal importance to enabling NuSTAR was developing hard X-ray position sensitive detectors. X-ray detectors employ a wide range of technologies ranging from gas proportional counters (e.g., in the upcoming *AstroSat*; Agrawal, 2006) to fine pixelled CCD detectors in focusing soft X-ray telescopes. However, these detectors have certain limitations (Section 2.1). Proportional Counter Arrays have to strike a trade-off between bulkiness and efficiency. Silicon detectors like CCDs are relatively transparent in the hard X-ray band. Some Coded Aperture Mask instruments use Cadmium Zinc Telluride (`CdZnTe`) detectors with large pixels for imaging. NuSTAR and other upcoming focusing hard X-ray telescopes require detectors with a pixel pitch less than a millimeter, without compromising on quantum efficiency or energy resolution. The development and calibration of such `CdZnTe` detectors at Caltech is the focus of the first half of this thesis.

1.3 NuSTAR

The Nuclear Spectroscopic Telescope Array (NuSTAR) is a NASA small explorer mission that will carry the first focusing hard X-ray optics into space (Harrison et al., 2010). With a pair of coaligned focusing telescopes (Figure 1.4), NuSTAR has an order of magnitude better angular resolution and is two orders of magnitude more sensitive than any existing hard X-ray instrument (Table 1.2, Figure 1.5).

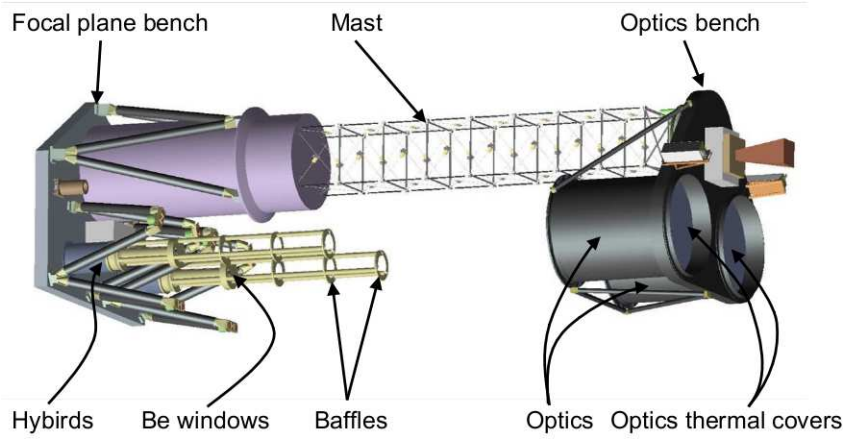

Figure 1.4. A schematic of NuSTAR. The satellite consists of two identical coaligned telescopes. Both optics are mounted on the "optics bench," which is connected to the "focal plane bench" by a deployable mast. The mast is in a stowed configuration at launch, and extends to 10.15 meters when deployed. Detectors (known as hybrids) are housed inside two focal plane modules which contain active shielding, readout electronics, and beryllium entrance windows. The optics are 38 cm in diameter.

NuSTAR was has four primary science goals:

1. Locate massive black holes,
2. Study the population of compact objects in the Galaxy,
3. Understand explosion dynamics and nucleosynthesis in core collapse and Type `Ia` supernovae,
4. Constrain particle acceleration in relativistic jets in supermassive black holes.

Table 1.2. Sensitivity of hard X-ray telescopes

Satellite (Instrument)	Energy range	Sensitivity
Integral (ISGRI)	20–100 keV	~ 500 μCrab (>Ms exposures)
Swift (BAT)	15–150 keV	~ 800 μCrab (>Ms exposures)
NuSTAR	10–30 keV	~ 0.7 μCrab (1 Ms)

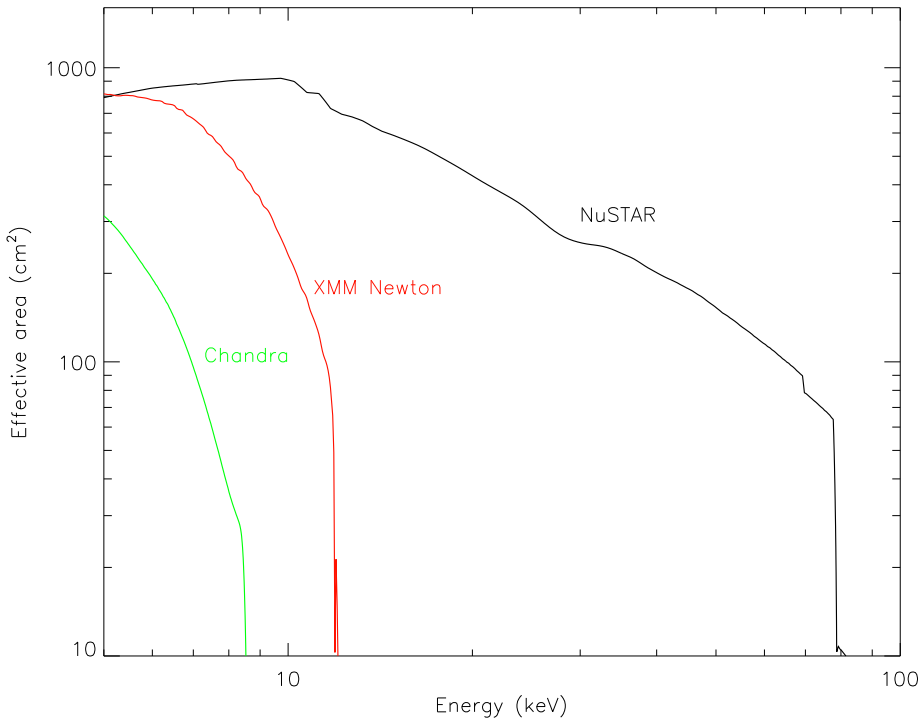

Figure 1.5. Comparing the NuSTAR effective area (both telescopes combined) to *Chandra* and *XMM-Newton* as a function of energy. NuSTAR utilizes a low graze angle design with depth-graded multilayer coatings to extend the sensitivity to 80 keV. The sharp cutoff at 80 keV is caused by a K-shell absorption edge in platinum used in the coatings.

In addition, the science team has identified several other compelling science programs (Table 1.3). Many of these science goals have been incorporated in the observing plan for the two year baseline mission. A Guest Observer (GO) program will be proposed at the end of the baseline mission to broaden the scientific output from the mission.

NuSTAR builds on the technology developed for the balloon mission "HEFT" (High Energy Focusing Telescope; Harrison et al., 2006). NuSTAR's performance is made possible by leveraging three key technological breakthroughs: efficient hard X-ray focusing optics, state-of-the-art `CdZnTe` detectors, and a deployable mast. Below I describe the telescope design in more detail.

NuSTAR employs low grazing angle focusing optics which are conical approximations to the Wolter-I design (Hailey et al., 2010). Each of the two optics modules on board the spacecraft has 133 concentric, confocal shells with a focal length of 10.15 m. Individual

optics shells are made by slumping glass on cylindrical mandrels. These sections are then clamped into place, with precisely machined graphite spacers that constrain the glass into the appropriate conical shape. The high energy reflectance of shells is enhanced by using multilayer coatings (Section 1.2). The coatings employ a combination of W/Si bilayers on the outer 43 shells, and Pt/C on the inner 90 shells. Pt has a K-shell absorption edge produces a sharp drop in the effective area at 79 keV.

Table 1.3: A representative list of NuSTAR science targets

Galactic plane survey	Magnetars	AGN physics
Sgr A*	X-ray binaries	Compton-thick AGN
Supernova Ia ToO	Pulsars	Blazars
Supernova remnants	Gamma-ray binaries	Starburst galaxies
Solar physics	Extragalactic surveys	Galaxy clusters
Flaring protostars	Ultraluminous X-ray sources	Radio galaxies
Planetary wind nebulae	Targets of opportunity (ToO)	ULIRGs

The optics have an angular resolution of $\sim$ 12″ (FWHM)[3], and a field of view of $\sim$ 10′. The reflectivity of optics shells starts decreasing with increasing angle of incidence of photons. This effect is more pronounced at higher energies and the field of view drops to 6′ at 60 keV (Figure 1.6).

Each telescope has a corresponding Focal Plane Module (FPM) consisting of four 32×32 pixel CdZnTe detectors. These detectors have energy resolution of $\sim 1\%$ and high quantum efficiency over the entire NuSTAR energy range. Detectors are discussed in greater detail in Chapter 2.

Small explorer (SMEX) missions are NASA's smallest astrophysics platform and the launch vehicle fairing cannot accommodate a fixed 10 m telescope. To overcome this limitation, the instrument is launched in a compact stowed configuration. After launch, a deployable mast developed by ATK Space Systems, Goleta[4] extends to achieve the 10.15 m focal length.

NuSTAR will be launched in the Summer of 2012 on a *Pegasus XL* rocket by Orbital

[3]The half power diameter (HPD) is $\sim 50''$.

[4]http://www.atk.com/capabilities_multiple/goleta.asp.

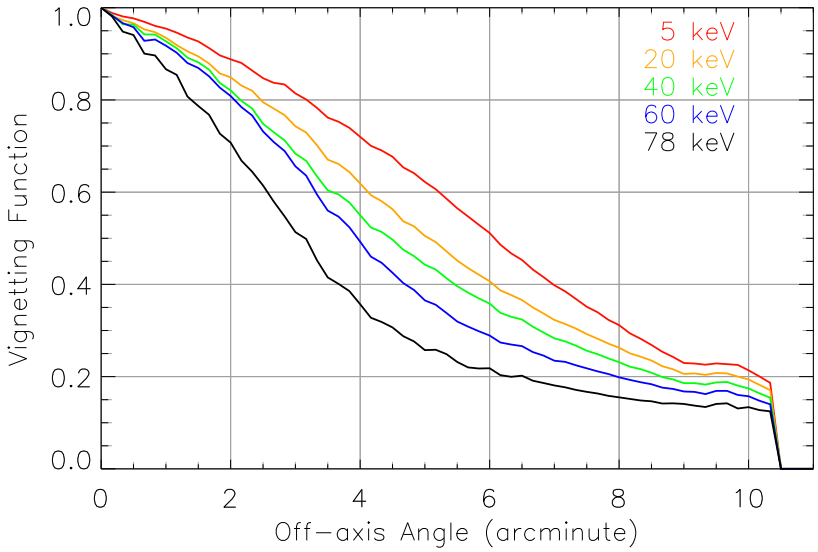

Figure 1.6. Off-axis response of NuSTAR as a function of angle, for various energies. The on-axis response is normalized to unity independently for each energy. The field of view is 10′ in diameter at 10 keV and decreases to about 6′ at 60 keV.

Sciences Corporation into a 6° inclination, 575 × 600 km Low Earth orbit. The orbit is selected to avoid passages in the South Atlantic Anomaly (SAA) where the concentration charged particles in the Earth's atmosphere increases, leading to high background noise. The low earth orbit results in frequent earth occultations for several targets. The satellite does not reorient during earth occultation, decreasing the observing efficiency to near 50% for most targets, leaving it closer to 90% for polar targets.

The mission has a nominal lifetime of 2 years, during which it will address primary science goals. This will include a few Target-of-Opportunity (ToO) observations with a response time of < 1 day. There are no consumables on board and the mission life is limited by the $\sim$ 10 year orbit decay timescale. The data will be downlinked to Malindi, Kenya, and transferred to the Mission Operations Center (MOC) at UC Berkeley. The Science Operations Center (SOC) at Caltech validates the data and converts it to FITS format conforming to OGIP standards. NuSTAR science data have no proprietary period, after a six-month interval to calibrate the instrument and verify performance, all data will be uploaded to the HEASARC[5] public archive within two months of completion of an observation.

[5]High Energy Astrophysics Science Archive Research Center; http://heasarc.nasa.gov/.

Chapter 2

Cadmium Zinc Telluride Detectors

I discuss the desired properties of hard X-ray detectors in Section 2.1, followed by specifics of NuSTAR `CdZnTe` detectors (Section 2.2). Section 2.5 deals with details of how a photon is processed and read out by NuSTAR hardware. The rest of the chapter discusses various aspects of data analysis: calculating event rates (Section 2.4), calculating photon energies (Section 2.5), and photon pileup (Section 2.6).

2.1 Hard X-ray Detectors

The performance requirements of detectors are driven by the scientific goals of a mission and the accessible technology. As NuSTAR is an imaging telescope, the primary requirement is to develop imaging detectors with a pixel pitch that optimally samples the point spread function (PSF) of the optics. The FWHM of the optics PSF is $\sim 12''$. At a focal length of 10 m, that translates to a physical size of ~ 600 μm. This requirement drives the pixel size of the NuSTAR detectors. We selected `CdZnTe` as the material of choice for NuSTAR detectors, to make compact, segmented detectors with good energy resolution. `CdZnTe` functions well at 0°–10° C, simplifying the readout electronics. These temperatures can be attained in orbit by passive cooling, thereby eliminating the need for cryogenics.

In hard X-ray, the dominant process by which photons interact with high-Z matter used in X-ray detectors is photoelectric absorption (Longair, 1992, Chapter 4). A photon of energy $h\nu$ can eject electrons with binding energies $E_i \leq h\nu$ from atoms. The energy levels in atoms for which $h\nu = E_i$ are called absorption edges, where the absorption probability of a photon increases sharply as it can interact with electrons from this energy level. For

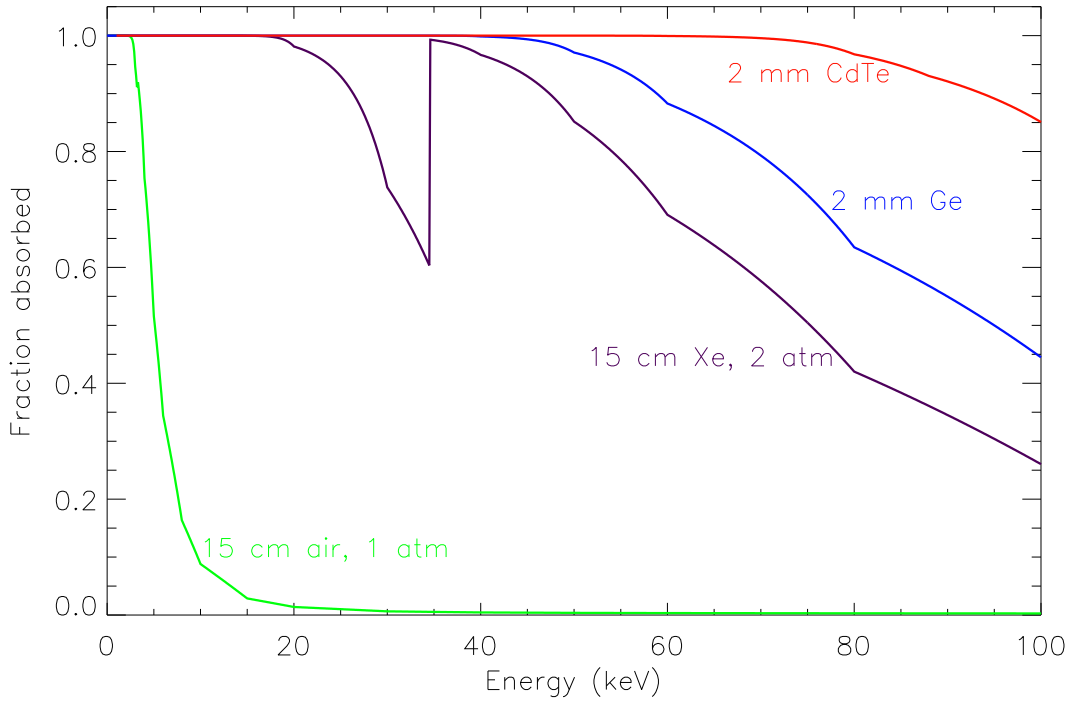

Figure 2.1. Comparing the X-ray absorption properties of various elements. The green curve shows the absorption by 15 cm of dry air at 1 atmosphere—this small air column is essentially transparent to X-rays above 10 keV. The purple curve is the absorption curve for 15 cm of `Xe`, similar to the gas-filled detector LAXPC on the upcoming Astrosat (Agrawal, 2006). The opacity rises sharply at the 34.5 keV K-edge for `Xe`. Solid state detectors like `Ge` (blue) perform better. A 2 mm thick `CdZnTe` crystal like ones used in NuSTAR hybrids absorbs almost all X-rays up to 80 keV (red curve, top).

example, `Xe` has an absorption edge at 34.5 keV (Figure 2.1). For photons with energies greater than the absorption edge, the cross section for photoelectric absorption from this level decreases roughly as ν^{-3}. At a given photon energy, the photoelectric absorption cross section also strongly depends on the atomic number (Z) of the material. At hard X-ray energies, the absorption cross section for K-shell electrons of atoms is proportional to the fifth power of the atomic number. Thus, `CdZnTe` (mean $Z = 49.1$[1]) absorbs hard X-rays above 10 keV better than, say, `Si` ($Z = 14$).

In a semiconductor detector, when a photon with energy $h\nu$ ejects an electron with

[1]Atomic numbers are `Cd` = 48, `Zn` = 30, `Te` = 52.

binding energy E_i, the remaining energy $h\nu - E_i$ is converted into kinetic energy of the ejected electron. Part of this energy is lost to the lattice of the substrate, but much of the rest of it serves to excite electrons from the valance band to the conduction band, creating thousands of electron–hole (e^-–h^+) pairs. The total number of e^-–h^+ pairs generated depends on the energy of the incoming photon and the characteristics of the substrate, in particular the band gap. Thus, we can calculate the energy of the incident photon by measuring the charge generated in the detector. This process of "event reconstruction" is discussed in more detail in Section 2.5.

Finally, another important consideration for X-ray instruments is the timing capabilities. The times of arrival of photons carry information about the emission characteristics of the source. For example, pulsations and periodicities in X-ray binaries can be analyzed to understand the properties of the compact object and orbital characteristics of the system. Typical count rates from astrophysical sources in the hard X-ray band are rather low: an X-ray source with a flux of about 1 mCrab gives about 10^{-4} photons cm^{-2} s^{-1} in the 15–50 keV band. With typical apertures of a few hundred square centimeters, the total count rates remain well within the processing realm of modern electronics.

In summary, a good hard X-ray detector should accurately measure the position, energy, and time of arrival for every X-ray photon that strikes it, while having high Quantum Efficiency (QE) and space-suitable features like compact geometry. Requirements for NuSTAR detectors are given in Table 2.1.

2.2 NuSTAR Detector Architecture

The Space Radiation Laboratory (SRL) at Caltech started developing hard X-ray detectors over a decade ago, for a balloon experiment named "High Energy Focusing Telescope" (HEFT; Harrison et al., 2006). The technologies developed for that first generation of detectors were adapted and refined to make NuSTAR detectors. NuSTAR has two focal plane modules, each consisting of four "hybrids" consisting of a `CdZnTe` crystal mounted on a custom integrated circuits (Figure 2.2). Each hybrid is an array of 32×32 pixels of 605 μm each. These sizes were determined from considerations of the smallest pixel size which can still incorporate the necessary circuitry, and the largest practical size of a uniform `CdZnTe` crystal. Hybrids assembled and selected for NuSTAR are designated by numbers, like H82,

Table 2.1. NuSTAR focal plane configuration summary

Parameter	Value
Pixel size	0.6 mm/12.3″
Focal plane size	$13' \times 13'$
Pixel format	32×32
Threshold	2.5 keV (each pixel)
Max processing rate	400 evt/s
Max flux meas. rate	10^4/s
Time resolution	2μs
dead-time fraction (weak source)	2%

H95, etc. Let us look at the two components of the hybrid to understand their basic working principles. For more details, see Iniewski (2010), Chapter 3.

The readout circuitry of the hybrid is a custom ASIC (Application Specific Integrated Circuit) developed at Caltech and manufactured by ON semiconductors. The ASIC fulfills the requirements for NuSTAR, with low power consumption, low readout noise, and a "rad hard by design" implemention to tolerate the space radiation environment. Each pixel contains a charge sensitive low-noise preamplifier, 16 sampling capacitors, a shaping amplifier, a discriminator, and a latch. The design also incorporate test probes like a programmable analog output for studying with oscilloscopes. A precision test pulsar in each pixel can be used to test the performance of the preamplifiers and measure linearity, offset, and noise characteristics. For NuSTAR, the ASIC is operated in a "charge pump mode," achieving very low electronic noise ($\sim$ 200 eV FWHM). In this mode, it can handle detector leakage currents up to 200 pA. The total noise of the electronics depends on the impedance in the feedback loop, where the capacitance is a dominant term. The detector crystal is directly bonded onto the ASIC, eliminating coupling networks and minimizing the input capacitance. To ensure that the input capacitance at the anode pads is lower than the parasitic capacitance between anode pixel pads (about 300 fF), the ASIC–crystal spacing

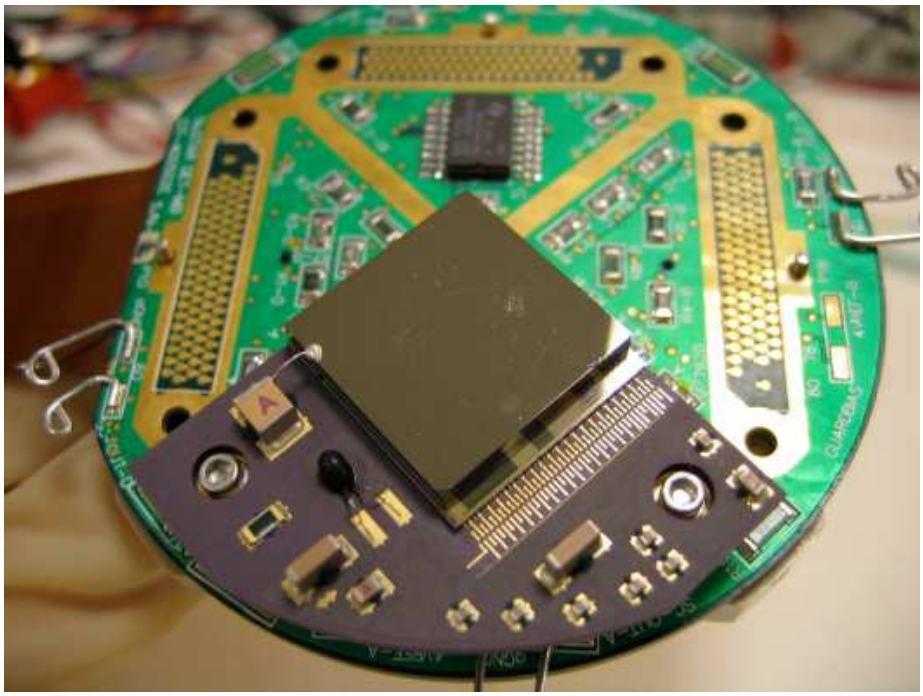

Figure 2.2. A NuSTAR hybrid (shiny square) mounted on a motherboard (green). The hybrid measures about two centimeters on a side. The top surface is the Pt cathode. A tiny wire from the capacitor "A" forms the connection for applying a negative high voltage. The three empty quadrants can hold one hybrid each.

needs to be ~ 50 μm. This spacing is achieved by bonding a gold wire to the ASIC input pad, and attaching the other side to the CdZnTe using a conductive epoxy. The ASIC is controlled by an external microprocessor. In NuSTAR, a MISC (Minimum Instruction Set Computer) and some peripheral state machines on an Actel FPGA (Field Programmable Gate Array) control the four ASICs in a Focal Plane Module.

The detector substrate is a 2 mm thick CdZnTe crystal, manufactured by eV microelectronics (now EI Detection & Imaging Systems[2]). The front surface seen in Figure 2.2 is a 1000 Å thick continuous Pt cathode. The anode contacts are a combination of about 1000 Å Pt and 3000 Å gold, laid out in a 605 μm pitch square grid matching the ASIC. Adjacent anode contacts are separated by 50 μm gaps. Unlike the familiar CCD (Charge Coupled Device) technology, there is no physical insulation within the semiconductor substrate between pixels. The segmented anode pattern forms the pixels in the detector. Having a larger spac-

[2] http://www.evmicroelectronics.com/

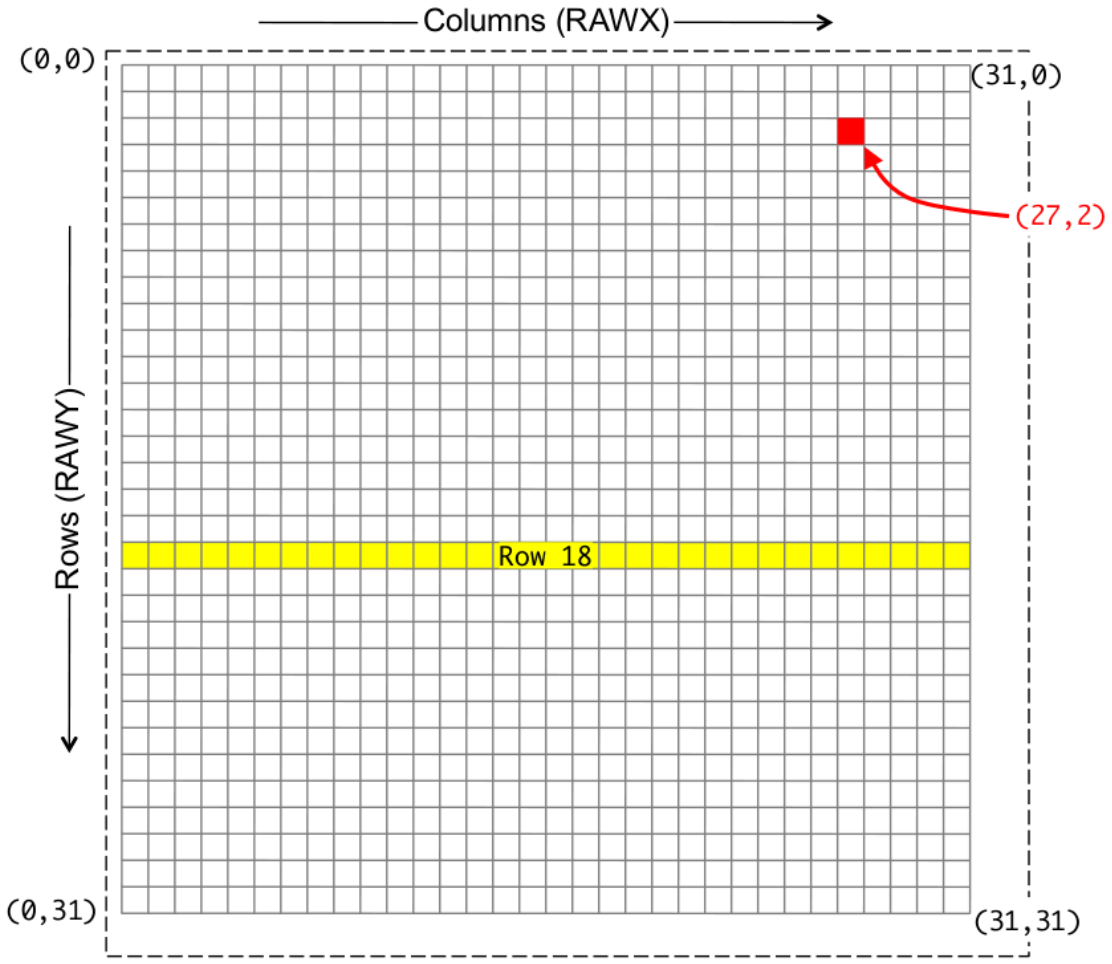

Figure 2.3. Schematic of a NuSTAR CdZnTe detector as seen from the top. The gray grid of squares mark the pixels, and the black dashed box is the physical boundary of the detector. The top and left edges are the "critical edges," intersecting at the critical corner. The four hybrids in a FPM are placed with their critical corners at the center. Row numbers increase from from 0 at the top to 31 at the bottom, and are also referred to as RAWY. The row with RAWY = 18 is highlighted as an example. Column (RAWX) numbers increase from left to right. Pixels are numbered as (COL, ROW) or (RAWX, RAWY)—for example the pixel highlighted in red is (27, 2).

ing decreases the parasitic inter pixel capacitance, and decreases noise—but leads to higher charge loss (Bolotnikov et al., 1999). Hence, we use the minimum possible gap dictated by EI's fabrication process. Near the edge of the detector, a guard ring with a tunable bias voltage steers the electric fields to the edge pixels. The detectors have two "critical edges," where the pattern is laid out close to the physical edge of the crystal with strict tolerance needs (Figure 2.3). This allows 4 hybrids to be placed together in a NuSTAR focal plane module with an effective gap less than a pixel. In normal operation, the cathode is biased at about −300 to −500 V with respect to the anode, using an external high voltage power supply.

2.3 Photon Trigger and Readout

To understand the working of the detector, let us consider a hard X-ray photon incident on the detector (Figure 2.4). It preferentially interacts with an inner-shell electron, eventually creating e^-–h^+ pairs as discussed in Section 2.1. For `CdZnTe`, the "effective band gap," or energy consumed per e^-–h^+ pair is about 4.85 eV. The electron cloud drifts towards the anode under the applied voltage. As the e^- cloud drifts, it expands due to diffusion and self-repulsion. The electrons follow the electric field and are collected on one or more anode pixel pads. The mobility of holes in `CdZnTe` is significantly lower than electron mobility, so the holes essentially remain frozen in place at the interaction site. They induce a mirror charge on the anode pixels, with opposite polarity as the electron signal.

A charge–sensitive preamplifier connected to each anode pads produces two outputs. A current output is sequentially routed to a bank of sixteen sampling capacitors in a round-robin fashion. The programmable sampling interval is normally set to $1\mu s$[3]. The second preamplifier output is a voltage signal proportional to the current. This output is fed in to a shaping amplifier with shaping time of approximately 0.5 μs. A discriminator compares the shaping amplifier output to an externally set voltage to generate a hardware trigger. This external voltage thus sets the trigger threshold, viz. the minimum charge deposit required to trigger a pixel. Due to manufacturing tolerances, this threshold corresponds to a slightly different photon energy for each pixel and needs to be measured during calibration.

[3]The onboard clock frequency is $f_{\rm clk} = 14.7456$ MHz. Each capacitor is connected for 15 clock ticks, giving $t_{\rm samp} = 15/f_{\rm clk} = 1.017$ μs.

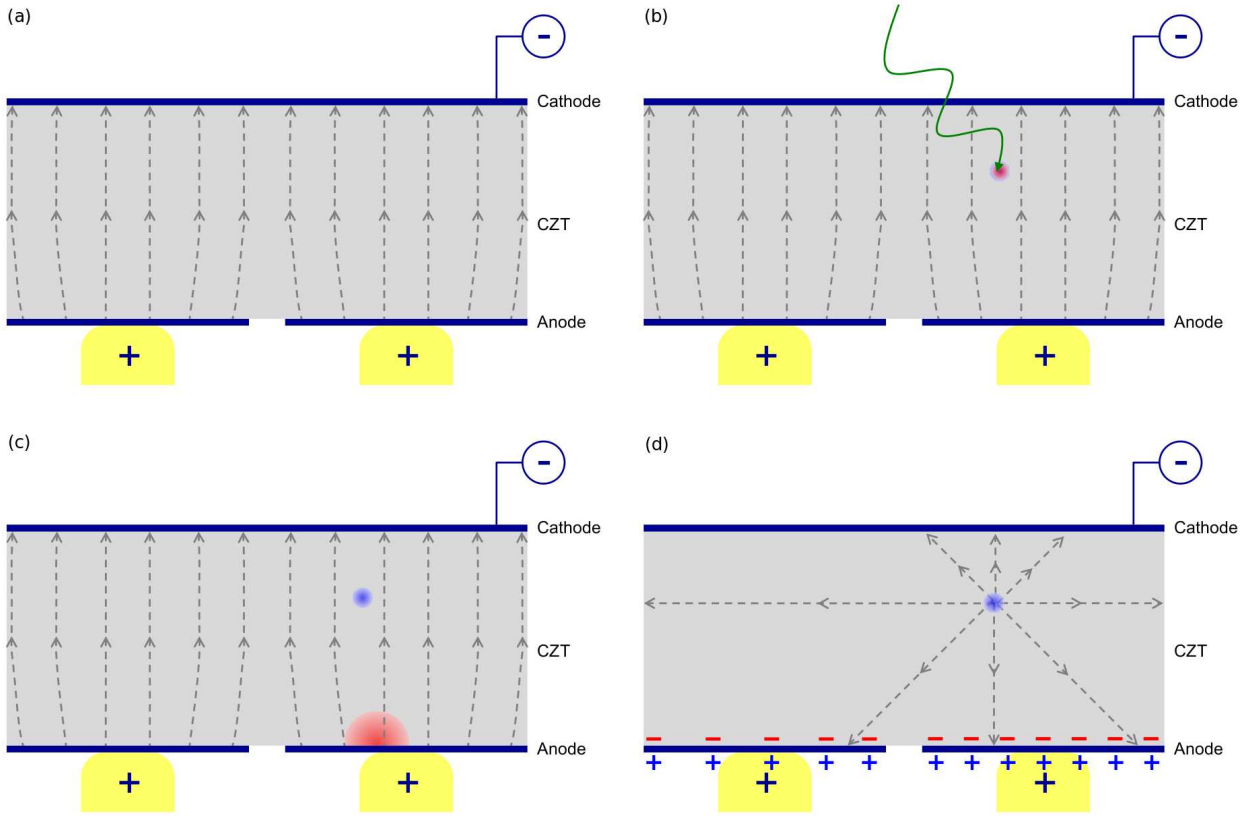

Figure 2.4. Working principle of `CdZnTe` detectors. (a) The NuSTAR hybrids consist of a `CdZnTe` crystal (shown in gray) with a continuous `Pt` cathode (blue, top), biased at −300 to −500 V with respect to a pixelled anode (blue, bottom). The anode contacts are shown in yellow. (b) An incident hard X-ray photon interacts to generate a charge cloud of e^-–h^+ pairs. (c) The electrons (shown in red) drift to the anode under the applied potential. The cloud expands due to diffusion and self-repulsion. Holes (light blue) remain frozen in-place. (d) Electric field created by the trapped holes, and the resulting induced charge on the electrodes. For simplicity, the electric field due to the applied voltage is not shown.

The hardware trigger for pixel is stored in a latch. These hardware triggers are sequentially combined in OR gates in a row to produce one trigger signal per row (at column 31). These 32 signals are combined in a OR gate into a single ASIC hardware trigger. The trigger outputs from all 4 ASICs are routed off-board to the FPGA, where all or a subset of them can be OR-ed to produce a FPM trigger signal. So far, the trigger processing is asynchronous. It is converted to a synchronous pulse in two clock ticks and fed to a state machine called the "pico processor" on the FPGA, which issues a "lockout" signal to stop processing further triggers in the ASICs. Thus, the "coincidence window" between the hardware trigger and the lockout signal is two to three clock cycles. We will revisit this number in Section 2.4. The round-robin sampling of capacitors is stopped after 6 more clock cycles, so that the capacitor banks have eight pre- and post- trigger samples each.

The MISC controls the processing and readout of the trigger. The event is rejected as a noise event if two hybrids triggered within the coincidence window. If the trigger was from a single hybrid, the MISC reads out a trigger map consisting of one bit per pixel, from the latch of each pixel. This map is then searched for hardware triggers starting from pixel (31, 31), progressing upwards along a column to pixel (31, 0), and repeating the procedure for columns 30–0. From charge sharing considerations, we expect that astrophysical hard X-ray photons will not deposit significant charge in more than four pixels. So, the search for hardware triggers is terminated after finding the first four triggers in this order. The number of processed triggers can be changed by a software setting.

At this point, the sixteen capacitors in each pixel hold 8 charge samples before the trigger and 8 after. We denote these samples by $s_0, s_1 - s_{15}$. In case multiple pixels triggered within the coincidence window, the sampling process stops after 8 clock ticks from the *first* hardware trigger. These capacitors are read out one by one to a charge-rebalance Analog-to-Digital Converter (ADC). To first order, the relation between the value read out and deposited charge is independent of the actual on-chip capacitances, making it robust to manufacturing variations. For each pixel, we calculate the pre- and post- trigger charge levels:

$$\texttt{PRE} = s_0 + s_1 + s_2 + s_3 + s_4 + s_5, \tag{2.1}$$

$$\texttt{POST} = s_9 + s_{10} + s_{11} + s_{12} + s_{13} + s_{14}. \tag{2.2}$$

The charge deposit in each pixel is calculated as the difference between the POST and PRE sums. The pixel with the highest charge deposit is selected as the central trigger pixel. The misc then reads out the eight nearest neighbors of only this pixel and calculates their PHAs. If any of the neighbors had hardware triggers, they have been read out already and are not processed again.

The exact time of the photon trigger within the 1 μs sampling window can be estimated by assuming a linear rise in deposited charge for the first few samples after the trigger. We calculate a weighted mean of these samples as the time-of-rise estimator, which is used later in event reconstruction to correct for the time shifts in the sampling that affect the energy measurement (Section 2.5). The estimator is defined as

$$\begin{aligned} \texttt{TOR} &= \frac{-3(s_6 - s_5) - 1(s_7 - s_6) + 1(s_8 - s_7) + 3(s_9 - s_8)}{(s_6 - s_5) - (s_7 - s_6) + (s_8 - s_7) + (s_9 - s_8)} \\ &= \frac{3s_5 - 2s_6 - 2s_7 - 2s_8 + 3s_9}{s_9 - s_5}, \\ \texttt{TOR} &= \frac{\texttt{NUMRISE}}{\texttt{DENRISE}}, \end{aligned} \tag{2.3}$$

where the 16 capacitor samples are numbered $s_0 - s_{15}$ as before. The MISC calculates the NUMRISE and DENRISE terms and the division is carried out in post processing.

Each photon event is packaged into an "event" and immediately sent to the Central MISC or central processor on board the NuSTAR satellite. The event data (Figure 2.5) contain all relevant event information, including

- Packet synchronization header.
- Column (RAWX) and row (RAWY) of the central pixel, number of the starting capacitor for the sixteen samples (S_CAP).
- FPM and detector number to identify among the eight hybrids on board NuSTAR.
- Timing information: Time since the once-per-second frame sync signal, live-time since last event, and time since last charge pump reset.[4]

[4] In charge pump mode, the feedback capacitor on the preamplifier is reset once every millisecond to remove any charge deposited by the leakage current. The pixel is marginally more susceptible to noise for a few microseconds after this reset.

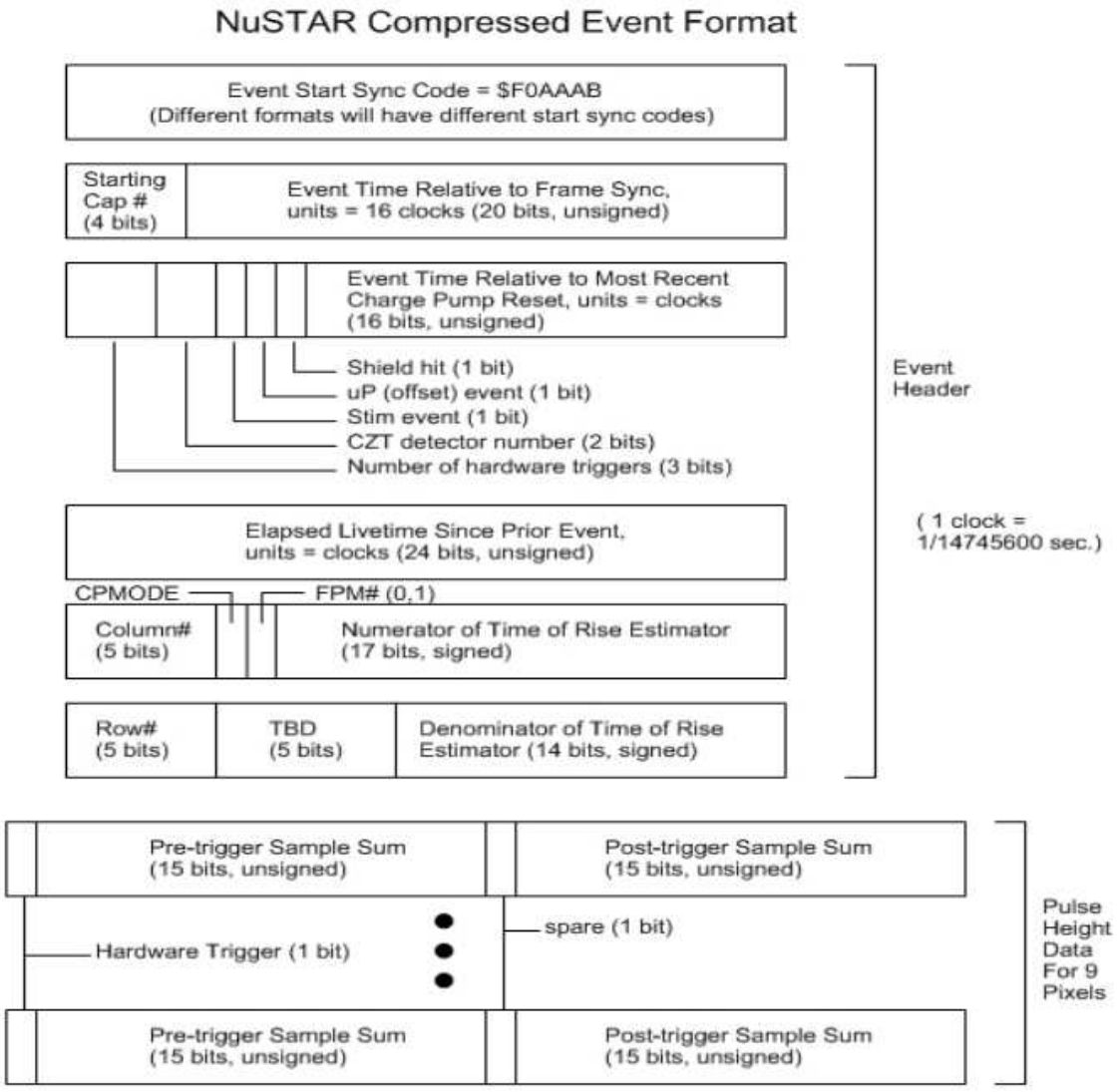

Figure 2.5. NuSTAR event data packet format. Event packets are 56 bytes long and contain all information about a photon event: the `PRE` and `POST` trigger sums, time of rise estimator, event timing information, pixel and detector ID, etc. (See Section 2.3 for a detailed description.)

- `NUMRISE` and `DENRISE` for the time-of-rise estimator.
- `PRE` and `POST` trigger sums for the central pixel and the 8 nearest neighbors.

The event time is referenced to a once-per-second sync signal from the spacecraft. Stability of the onboard clocks allows relative timing accuracy of tens of microseconds. The absolute timing accuracy of NuSTAR is $\sim$ 100 ms, determined by the spacecraft to UTC time synchronization.

The MISC can reject certain types of events based on programmable criteria. Any events with photons detected on two hybrids within the coincidence window are rejected as they likely originate from a particle shower induced event. The PMT (Photomultiplier tube) in the active `CsI` shield generates SHIELDHI and SHIELDLO signals when it detects light above a high and low threshold respectively. A SHIELDHI trigger corresponds to high amplitude signal generated in the PMT. Hence, the anticoincidence window is digitally stretched to 500 μs to allow sufficient time for the PMT to stabilize again before starting event processing again. These signals are digitized and processed by the MISC, where an algorithm computes whether any photon event should be vetoed based on the shield triggers. The MISC software can be set to either discard rejected events or to transmit them in special rejected event packets that contain only relevant information, like time since previous event.

The MISC then resets all latches, initiates the round-robin sampling of capacitors and the detector becomes live again after 8 samples. The entire readout process takes 2.50 ms. Any new photon events during this window are not processed. In other words, the detector is "dead" during this time, an effect discussed in detail in the next section.

2.4 live-time, dead-time, and Event Rates

As discussed in Section 2.3, there is a $\tau_D \approx 2.50$ ms dead-time window in the focal plane after a photon trigger, when that event is being processed. During this window, the focal plane does not trigger on any other incident photons. At low count rates, this does not significantly alter the inferred count rate or spectrum. If the incident rate on a focal plane (4 detectors combined) is high, then it is likely that photons will be incident on the detector during the dead-time windows. These photons are lost as they do not trigger the detector

(Figure 2.6).

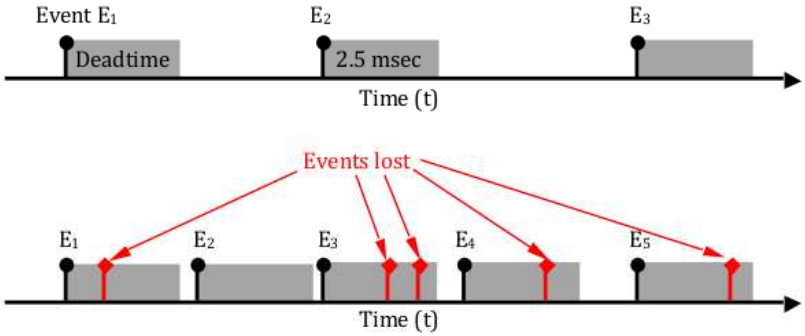

Figure 2.6. Top: Events (E_i) triggering the detector at a low count rate. Gray rectangles denote dead-time windows during which the event is processed. At low count rates, there is a very low probability of receiving photons in the dead-time interval following any trigger. Bottom: At higher count rates, several photons (shown in red diamonds) are incident during the dead-time intervals, and are lost. The measured count rate is thus lower than the incident count rate.

This effect starts becoming significant when the incident count rate R_i becomes high enough that the mean time between events is comparable to the dead-time τ_D. The limiting case is where the detector is triggered as soon as it goes live—this corresponds to $R_{i,\mathrm{crit}} \sim \tau_D^{-1} = 400$ counts s^{-1}.

Since the detector can detect incident photons only in "live" intervals, the incident count rate R_i is given by

$$R_i = \frac{\text{Number of photons}}{\text{Live time}}. \tag{2.4}$$

If we observed N_o photons in a time interval Δt, then the live-time is $t_{\mathrm{live}} = \Delta t - N_o \tau_D$. Substituting this in Equation (2.4), we get

$$\begin{aligned} R_i &= \frac{N_o}{\Delta t - N_o \tau_D} \\ &= \frac{N_o/\Delta t}{1 - (N_o/\Delta t)\tau_D} \\ &= \frac{R_o}{1 - R_o \tau_D}, \end{aligned} \tag{2.5}$$

where $R_o = N_o/\Delta t$ is the observed (measured) count rate. Equation (2.5) can be inverted

to calculate R_o from R_i:

$$R_o = \frac{R_i}{1 + \tau_D R_i}. \tag{2.6}$$

The transformation between R_i and R_o is given in Table 2.2 and plotted in Figure 2.7.

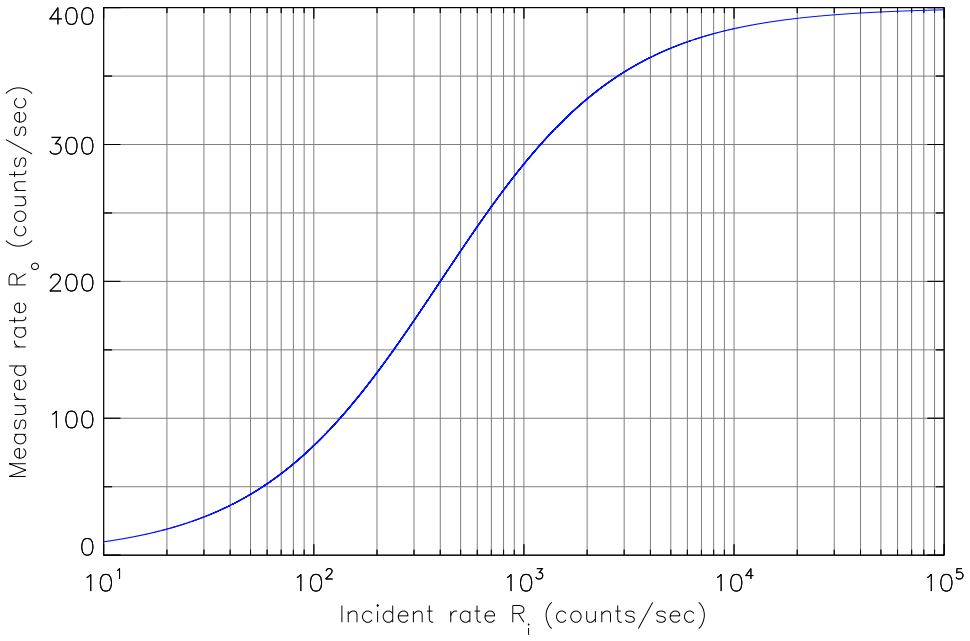

Figure 2.7. Count rate conversion: each event trigger in NuSTAR hybrids is associated with 2.5 ms dead-time. As a result, the measured count rate is a nonlinear function of the incident count rate (Section 2.4, Table 2.2).

Apart from the basic conversion above, there are other effects like rejected events, charge pump resets, and shield veto events which can contribute to detector dead-time. In practice, the count rate is calculated by one of two methods. First, the MISC maintains a live-time counter which, as the name suggests, counts the number of clock ticks for which the detectors were live in a given second. A slight downside to this approach is that only one second averages of live-time are available.

The second method is to calculate the livetime from event data itself. The event data for every photon contains the live-time since last event, known as `PRIOR` (Figure 2.5). Adding up the `PRIOR`s from all event packets, in principle, gives the total live-time of the detector. However, this is complicated slightly because of rejected events. Consider a case where a photon event is rejected because of multidetector hits or a shield veto. The MISC sends

Table 2.2: Observed count rate (R_o) as a function of incident count rate (R_i).

R_o	20	50	75	100	150	180	200	220	240
R_i	21	57	92	133	240	327	400	489	600
R_o	250	260	270	280	290	300	310	320	330
R_i	667	743	831	933	1055	1200	1378	1600	1886
R_o	340	350	360	370	380	385	390	395	399
R_i	2267	2800	3600	4933	7600	10,267	15,600	31,600	159,600

Note. — The incident count rate R_i is for ground calibrations, and does not include effects like shield vetos which are expected in orbit.

a lockout signal, starts processing the event, and decides to veto it. The detector remains dead for less than the nominal 2.5 ms window. However, this resets the "time since last event" counter. As this event did not enter the data stream, the associated dead-time is not counted when we add up the PRIORs for all accepted events. Rejected event packets, if enabled, contain the live-time prior to each rejected event. Combining this information from accepted and rejected events, we can also calculate the dead-time associated with processing each rejected event. Using all this information we can calculate exact incident count rates.

2.5 Event Reconstruction

The raw spacecraft telemetry packets ("Level 0" data) are converted to produce scientific products ("Level 3") through several stages of processing (Table 2.3). Here, I describe the processing algorithms for calculating the energy of the incident photon using data from the event packets. For analyzing NuSTAR data, these algorithms are implemented in the NuSTAR Data Analysis Software (NuSTARDAS).

The data for each event contains the pre- and post- trigger sums for the trigger pixel and its eight nearest neighbors. First, we calculate the RAWPHAS from these values,

$$\texttt{RAWPHAS}[9] = \texttt{POSTPHAS}[9] - \texttt{PREPHAS}[9]. \tag{2.7}$$

Table 2.3. Data-processing overview

Stage	Name	Description	Output
1	Data Calibration	Processing of FITS formatted Level 0 telemetry	Level 1a calibrated unfiltered event files
2	Data Screening	Filtering of the calibrated event files by applying conditions on specified attitude/orbital/instrument parameters	Level 2 cleaned event files
3	Products Extraction	Extraction of high-level scientific products (images, light-curves, spectra, exposure maps) from cleaned event files	Spectra, light-curves, images, exposure maps

In this discussion, we use the suffix [9] for parameters which are stored separately for each of the nine pixels read out. The relation between the deposited charge and the ADC output varies slightly from capacitor to capacitor. We correct for this effect by subtracting offsets (OFFSET[9]) calculated for the starting capacitor S_CAP for every pixel.

$$\texttt{OFFPHAS}[9] = \texttt{RAWPHAS}[9] - \texttt{OFFSET}[9] \tag{2.8}$$

We apply a time-of-rise correction to remove the effect of exact time of incidence of the photon within the 1 μs sampling interval. For this, we use the NUMRISE and DENRISE terms calculated by the MISC, and a table of TIMERISE coefficients measured for each pixel:

$$\texttt{TRPHAS}[9] = \texttt{OFFPHAS}[9] \times \left(1 + \frac{\texttt{NUMRISE}}{\texttt{DENRISE}} \times \texttt{TIMERISE}[9]\right). \tag{2.9}$$

Next, we apply the "common mode correction" to calculate PHAS. The signal seen by a trigger pixel is the number of electrons collected by that pixel, less the hole charge imaged on that pixel (Figure 2.4). We separate pixels which have charge contributions from the photon (type "$E+$") from type "$E-$" pixels that see only the imaged hole charge. We estimate the hole charge signal from the $E-$ pixels and use it to correct the $E+$ signal. Note that the sign convention here refers to the energy deposited. The actual polarity of the signal is negative because the hybrids read out an electron signal (Section 2.3). The boundary between $E+$ and $E-$ signals, known as the software trigger threshold (EVTTHR), is determined empirically for each pixel. The 9 pixels are divided into three distinct groups: M pixels that are located outside the detector (for edge pixels) or are bad / hot pixels; N pixels (type "$E+$") with $\texttt{TRPHAS}[9] \geq \texttt{EVTTHR}[9]$; and $9 - N - M$ pixels (type "$E-$") with $\texttt{TRPHAS}[9] < \texttt{EVTTHR}[9]$. The common mode noise term is calculated as

$$\langle E- \rangle = \frac{\Sigma E-}{9 - N - M}. \tag{2.10}$$

We apply this correction only to the "$E+$" pixels, to get

$$\texttt{PHAS}[9] = \texttt{TRPHAS}[9] - \langle E- \rangle. \tag{2.11}$$

Values for the $9-N-M$ type "$E-$" pixels are left unchanged ($\texttt{PHAS}[9] = \texttt{TRPHAS}[9]$), while

the M outside/bad pixel values are zeroed out (PHAS[9] = 0). Similarly, we also compute SWTRIG[9] for pixels, such that SWTRIG[9] = 1 for the "$E+$" pixels and SWTRIG[9] = 0 for others. We calculate the scalar SURR by adding together the PHAS[9] for pixels with SWTRIG[9] = 0.

This is followed by assigning a GRADE from 0 to 31 to each event, based on the morphology of the SWTRIG[9] map (Figure 2.8). All these steps are implemented in the nucalcpha module of NuSTARDAS.

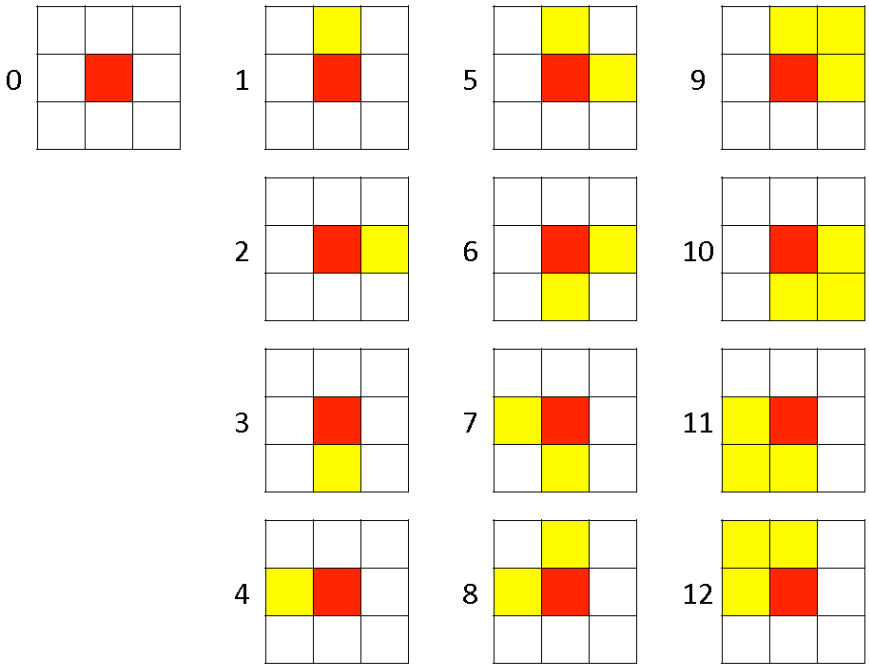

Figure 2.8. Grades are assigned to multiple pixel events based on the morphology of triggered pixels. The pixel grid is oriented as in Figure 2.3. In each case, the central pixel (red) is the one with the highest energy deposit. The nearby pixels shown in yellow have energy deposit higher than the software trigger threshold, and optionally greater than the hardware trigger threshold. Typically, about 90%–95% photon events in NuSTAR hybrids fall under the grades 0–12 shown here.

Next, we convert the PHAS into PIs in three steps. PI (Pulse Invariant) is expressed in units of 40 eV. This number was selected to be a factor of few smaller than the energy

resolution of NuSTAR detectors. First, we use the grades to apply pixel- dependent gain and offset corrections to PHAS[9]:

$$\texttt{PI}'[9] = \texttt{PHAS}[9] \times \texttt{GAIN}[9] + \texttt{OFFSET}[9]. \tag{2.12}$$

The PI′ calculation requires interpolation of coefficients in temperature and time. First, the two temperature measurements (in satellite housekeeping data) closest in time to the instant of the photon interaction are identified. For each of these two temperature measurements, a GAIN and OFFSET value is calculated by interpolating between tabulated GAIN, OFFSET values from the two nearest temperatures. The final GAIN[9] and OFFSET[9] values are calculated by interpolating with respect to time between these two coefficients.

The second step is to apply a charge loss correction for event grades 1–8 (two- and three-pixel events), based on the relative amount of charge deposited in the pixels. For grades 1–4, the corrected energy (PI) is given by Equation (2.13):

$$E_{corrected} = rA(\sin\phi + \cos\phi), \tag{2.13}$$

where

$r = \sqrt{E^2_{\text{center}} + E^2_{\text{second}}}$,
E_{center} is the grade 0 gain corrected PHA for the center pixel,
E_{second} is the grade 0 gain corrected PHA for the side pixel,
$\phi = \tan^{-1}(E_{\text{second}}/E_{\text{center}})$,
$A = C_{[X,Y,G]} \times \sin(2\phi)$,
$C_{[X,Y,G]}$ are charge loss correction coefficients for each column (X), row (Y), and grade (G) combination, for grades 1–4.

A fraction of high energy photons cause fluorescence events. In this case, the incident photon interacts in the detector to deposit some energy in a pixel, releasing a Cd or Te florescence photon. This photon may travel to an adjacent pixel and deposit energy in it. Since this is not the same phenomenon as the typical two pixel events, we do not apply a charge loss correction for fluorescence events. So, if $E_{\text{second}} = (26.7112 - 1.0) \pm 0.5$ keV (Cd) or $(31.8138 - 1.0) \pm 0.5$ keV (Te) then $E_{corrected} = E_{\text{center}} + E_{\text{second}}$.

For three pixel events of grades 5–8, the procedure is modified a bit:

$$E_{\rm corrected} = E_{\rm center} + r_1 A_1 \sin\phi_1 + r_2 A_2 \sin\phi_2, \tag{2.14}$$

where,

$r1 = \sqrt{(E_{\rm center} + E_{\rm third})^2 + E_{\rm second}^2}$,
$r2 = \sqrt{(E_{\rm center} + E_{\rm second})^2 + E_{\rm third}^2}$,
$E_{\rm center}$ is the grade 0 gain corrected PHA for the center pixel,
$E_{\rm second}$ is the grade 0 gain corrected PHA for the pixel with second highest PHA,
$E_{\rm third}$ is the grade 0 gain corrected PHA for the pixel with third highest PHA,
$\phi_1 = \tan^{-1}(E_{\rm second}/(E_{\rm center} + E_{\rm third}))$,
$\phi_2 = \tan^{-1}(E_{\rm third}/(E_{\rm center} + E_{\rm second}))$,
$A_1 = C_{[X,Y,G]} \times \sin(2\phi_1)$,
$A_2 = C_{[X,Y,G]} \times \sin(2\phi_2)$,
$C_{[X,Y,G]}$ are charge loss coefficients for grades 1–4 as above.

The charge loss coefficient depends only on the two pixels used in calculating A_i. Hence, even for charge loss correction to grades 5–8, we use the same charge loss coefficients as grades 1–4.

For all other grades (grade 0, grade > 12), we simply sum the $E+$ pixels to get $E_{\rm corrected}$ without applying a charge loss correction. For example, for four pixel events (grades 9–12), the final energy is calculated as

$$E_{\rm corrected} = E_{\rm center} + E_{\rm second} + E_{\rm third} + E_{\rm fourth}. \tag{2.15}$$

The third and final step to calculate PI values is to correct for gain, and apply a fixed offset:

$$\texttt{PI} = E_{\rm corrected} \times \texttt{GAIN}' + \texttt{OFFSET}_0. \tag{2.16}$$

$\texttt{GAIN}'$ values are tabulated for each grade for each pixel. PI are expressed as integer values in units of 40 eV. In addition, $\texttt{OFFSET}_0$ is subtracted from the "grade gain corrected energy" so that $\texttt{PI} = 0$ corresponds to an energy of 1.6 keV.

As mentioned before, the measured charge at pixel anodes is affected by the imaged

hole signal. For photons with a given energy, as the depth of photon interaction in CdZnTe increases, the hole contribution increases, reducing the total energy. The common mode correction does not completely remove this effect. However, we can use the total hole signal in $E-$ pixels to estimate the depth of interaction. So, we calculate a scalar SURRPI to make it available for the science user for filtering on depth cuts:

$$\texttt{SURRPI} = \texttt{SURR} \times \texttt{GAIN} + \texttt{OFFSET}, \tag{2.17}$$

where GAIN and OFFSET values for the central pixel are used.

After applying all these corrections, we obtain an events list with photon energies in PI units. Figure 2.9 shows laboratory spectra of radioactive elements measured by a NuSTAR CdZnTe hybrid. The uncertainty in energy arises primarily from three terms: electronic noise, Fano noise, and charge transport effects. Using the precision test pulsar in the ASIC, we have measured the electronic noise associated with the readout procedure to be $\approx$ 250 eV (FWHM) per pixel. This includes a contribution from leakage current flowing in CdZnTe due to the applied high voltage. Fano noise is the variation in $N_{\pm}$, the number of e^-–h^+ pairs created by a photon of fixed energy incident on the detector. The noise is typically less than noise expected from Poisson statistics. This is described by the "Fano factor" F, defined such that $\Delta E/E = \sqrt{F/N_{\pm}}$. For example, a 60 keV photon generates $N_{\pm} = 60$ keV/4.85 eV $\approx$12,400 e^-–h^+ pairs. Using $F \sim 0.1$ (Harrison et al., 2008; Niemela & Sipila, 1994), the uncertainty in the calculated photon energy is $\Delta E \approx 170$ eV. Charge transport effects arising from nonuniformity of the CdZnTe substrate dominate the uncertainty in energy reconstruction. Using only single pixel events ($\sim 1/2$ of all events), we attain an energy resolution of < 600 eV FWHM at 60 keV and 1 keV FWHM at 86 keV on NuSTAR hybrids. Including two-, three-, and four-pixel events in analysis slightly worsens the energy resolution.

The final step in event reconstruction is to calculate the detector coordinates for each photon events. This is done using the spatial probability distribution for event grades for each pixel, measured in ground calibration (Section 3.5). The probability distribution for event grades 0–12 is tabulated as a 7×7 grid in the Focal Plane Bench coordinate system, DET1. The DET1 system uses integer coordinates with pixel size corresponding to $12''.3/5$ at the focal plane. For each event, we assign (DET1X, DET1Y) coordinates based on the

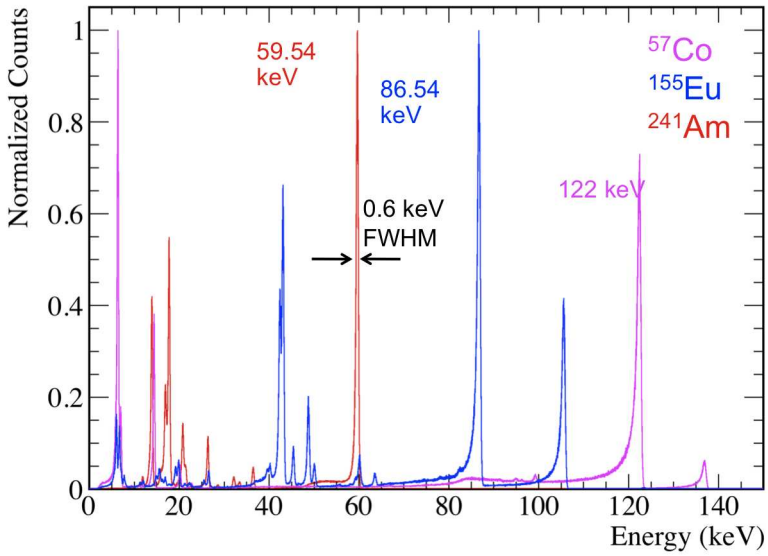

Figure 2.9. Radioactive source spectra measured by a NuSTAR `CdZnTe` hybrid. Independently acquired spectra for ^{57}`Co`, ^{155}`Eu` and ^{241}`Am` are plotted together, with peak counts normalized to unity. Only grade 0 events were used for making these spectra. All radioactive lines show a sharp core with some tailing towards lower energies. The core of the 59.54 keV ^{241}`Am` line has a FWHM of 600 eV. We obtain an energy resolutions of 400 eV at 6 keV.

probability distribution for the corresponding (`RAWX`, `RAWY`, `GRADE`) combination. These coordinates are later converted to the Optics Bench (`DET2`) using the mast aspect solution, and eventually to `SKY` coordinates.

2.6 Pileup

Pileup refers to two photons being incident on a detector in such a short duration, that they are read out as a single photon of higher energy. Pileup is not a major concern for pixelled detectors. However, for bright point sources, photons are incident at a high rate in a few pixel region of the detector, creating the possibility of pileup. Pileup was seen in laboratory measurements with the X-ray generator (Section 3.5) and the ^{55}`Fe` QE scans (Section 3.6).

Suppose a photon is incident on a detector pixel "A" at time $t = t_0$. We consider four time windows for the purpose of pileup:

1. *Trigger to lockout*: This time window spans the first 2 – 3 μs from the asynchronous

photon trigger to the MISC issuing a lockout signal to stop further triggers. A second photon incident in this duration on one of the 9 pixels to be read out will cause a hardware trigger. This is indistinguishable from a split pixel event arising from a photon with roughly the energy of both photons combined. This mode of pileup becomes important when the mean interval between photon arrival is a few times the coincidence window. In other words, $R_{\rm pile} \sim 1/(\text{few} \times 2\ \mu\text{s}) \sim 10^5$ counts/s.

2. *Lockout to end of sampling*: In the interval from $(t_0 + 3\ \mu\text{s})$ to $(t_0 + 8\ \mu\text{s})$, the hybrid will not issue any hardware triggers. However, if another photon is incident on one of the 9 pixels which will eventually be read out, then charge deposited by the photon still contributes to the POST sample sum for that pixel. Such events start occurring at count rates a few times lower than $R_{\rm pile}$. They can be screened out in careful postprocessing by searching for pixels which have enough energy deposited to cause a hardware trigger, but did not actually have a hardware trigger. Note that a few pathological cases are possible where this screening procedure will not identify such events. For example, if the second photon was incident next to the trigger pixel at $t \approx t_0 + 6\ \mu$s, it may raise the POST sum to a level between the hardware and software trigger thresholds. This will be missed by the screening procedure but will raise the measured energy of the event (pileup).

3. *End of sampling to just before detector live*: Any photons incident from $(t_0 + 8\ \mu\text{s})$ to $(t_0 + 2.5\ \text{ms} - 8\ \mu\text{s})$ neither trigger the hybrid, nor contribute to the energy deposited in the event.

4. *Last 8 μs of dead-time*: Consider the case where photon "P" is incident on pixel "A" within 8 μs of the detector going live. The PRE sum for that event contains some capacitor samples while the detector was still dead. If a photon "Q" was incident on one of the 9 pixels (say, pixel "B") during those samples, then it would not trigger the detector. But, the charge deposited by that photon still contributes to the PRE samples for that pixel. Such events start occurring at count rates a few times lower than $R_{\rm pile}$, and their consequences are slightly complicated. If photon P does not deposit any energy in pixel B, then the POST $-$ PRE value for this pixel will actually be negative. This will *add* some extra energy to PHA of the triggered pixel A when we

apply the common mode correction (Equation (2.11)). Like case 2 above, this can be screened out in postprocessing. On the other hand, if photon P deposited significant charge in pixel B, then the measured POST − PRE value will be lower than the true energy deposited in that pixel. Whether this can be screened out or not depends on the energy deposited by both photons in pixel B.

Most astrophysical sources will have count rates significantly lower than $R_{\rm pile}$ and these effects can be safely ignored. However, we will also carry out simulations to estimate the magnitude of these effects for NuSTAR observations of bright point sources.

Attaining the best performance from each hybrid requires careful calibration in the laboratory, a procedure which took a few hundred hours per flight hybrid. In the next chapter, I discuss the details of this calibration procedure.

Chapter 3

Calibration

Let us follow the optical path of an astrophysical source photon as it makes its way to a NuSTAR detector. The photon first passes through the optics thermal cover. Then it is reflected twice by the optics, and passes through the back thermal covers. The optics reflectivity has a sharp cutoff at 79 keV due to the K-edge of `Pt`. Closer to the focal plane, there are baffles which stop most of the stray light from near the field, which did not make it through the optics (Figure 3.1). The photon then passes through `Be` windows mounted on top of the detectors. These windows absorb lower energy photons ($\lesssim$ 3 keV)—this is important to keep the count rate reasonable by letting only photons in the energy range of interest reach the detectors. Finally, the photon interacts with the `CdZnTe` crystal and triggers a pixel. This initiates readout, and a photon event data packet is created and handed off to the spacecraft.

Each element of NuSTAR that a photon interacts with needs to be calibrated with great care in the laboratory to fully characterize the performance of the telescope. The degree of certainty in calibrations reflects directly on the quality of scientific output of the mission. In Section 3.1, I describe the performance requirements for NuSTAR and how they lead to calibration requirements at the component level. In Section 3.2, I discuss the calibration steps for every hybrid. In the remainder of this Chapter, I discuss all steps that I executed as a part of the hybrid calibrations, followed by transparency calibrations for the `Be` windows and optics thermal covers.

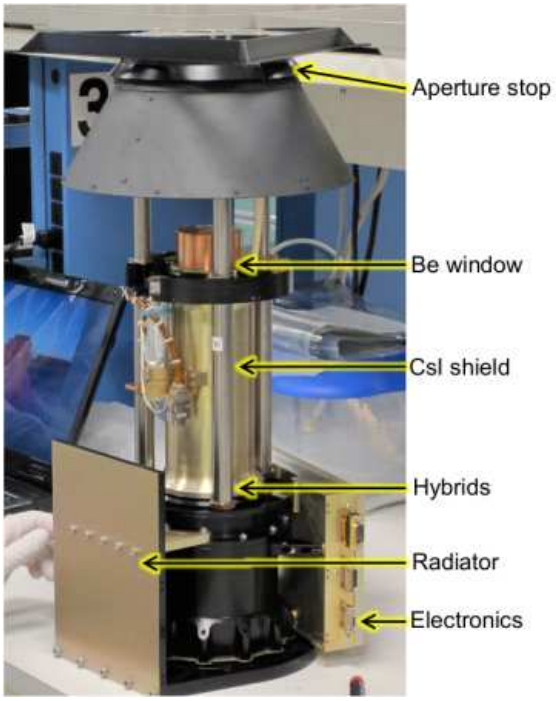

Figure 3.1. A NuSTAR focal plane module. The deployable aperture stop (top, black) sits on three telescoping rods. A copper can holds the Be windows, which block low energy photons. A CsI anti-coincidence shield surrounds the assembly, and a photomultiplier tube under the hybrids monitors any scintillation events in the shield. The hybrids are enclosed near the base of the golden assembly. On the left, a radiator passively cold-biases the entire module, heaters near the hybrids maintain operating temperature ($\sim$ 5°C). Control electronics are mounted on the right.

3.1 Requirements

Calibration requirements for NuSTAR are laid out from the primary science objectives. In brief, the relevant requirements are:

- **Absolute flux calibration**: For a source with a power-law spectrum with a photon spectral index of 1.7, the systematic uncertainties in flux should be less than 30% (3-σ) over the central $11' \times 11'$ of the field of view (FOV), and less than 15% in the 6–10 keV band in the central $2' \times 2'$. In order to accurately measure ^{44}Ti lines, the systematic uncertainty in absolute flux measurements should be $< 15\%$ in the 60–79 keV band in the central $8' \times 8'$.

- **Spectral calibration**: For a source with a power law spectrum of the form $F = kE^{-\alpha}$, $-1 < \alpha < 1$ the systematic error in measuring α should be less than 0.15 (3-σ) in the 6–10, 10–30, and 30–79 keV bands over the central $11' \times 11'$ of the FOV. In the 60–79 keV band, the uncertainty should be < 0.15 in the central $8' \times 8'$ of the FOV.

- **Point spread function characterization**: The integrated value of the instrument Point Spread Function (PSF) from 70%–90% encircled energy should be determined to 10% (3-σ) over the central $11' \times 11'$ of the FOV. The radial and azimuthal variations of the PSF (70% encircled energy) should be characterized to 3% and 10% (3-σ) accuracy respectively, over the central $11' \times 11'$ of the FOV.

The instrument level requirements derived from these calibration requirements are listed in Table 3.1. This is the net performance requirement for NuSTAR, including ground-based and in-orbit calibrations, in order to meet the science objectives. The motivation for defining the energy range for NuSTAR is to obtain hard X-ray spectra that complement existing soft X-ray data, without leaving behind any gap in the spectrum. This desire to have a sufficient energy overlap with soft X-ray missions drives our calibration requirements at the low energy end (6–10 keV). At the highest energies (60–80 keV), one of the science goals is to study the ^{44}Ti line emission in young supernovae remnants. To properly analyze the lines, we need to characterize the underlying continuum well, and in turn must understand the telescope response with high accuracy with good energy resolution. Requirements on characterizing the PSF stem from the aim of accurately understanding point images to study diffuse emission around them in the galactic plane.

It is impossible to measure the performance of the instrument at every possible combination of energy, incident angle, etc. Instead, we have very detailed models and simulations for each component of NuSTAR. The aim for ground and in-orbit calibration is to obtain select data sets to fit for a few model parameters, and verify the model. For example, the optics are illuminated with an intense X-ray beam at a range of angles, and the data are used to fit and verify a raytrace model. For the hybrids, the event reconstruction described in Section 2.5 are based on working knowledge of the electronics, and a charge transport model for CdZnTe.

Table 3.1. Instrument-level calibration requirements

Topic	Requirement	Rationale
Alignment		
Optical Axis Knowledge	15″	Throughput determination
Effective Area		
Absolute effective Area: 6–10 keV (central $2' \times 2'$)	15%	Cross calibration with low-energy missions
Absolute effective area: 6–10, 10–30, 30–79 keV bands ($11' \times 11'$)	25%	Hardness ratio determination and surveys
Absolute effective area in each 2 keV bin between 60 and 80 keV	12%	^{44}Ti yield measurement
Relative effective area in each 2 keV bin between 6 and 79 keV over central $8' \times 8'$	5%	Spectral index fitting and bright sources
Relative effective area in each 2 keV bin in the 60–79 keV range in central $8' \times 8'$	3%	Continuum modeling and subtraction for ^{44}Ti
Point Spread Function		
Integrated PSF 70–90% encircled energy over $11' \times 11'$	10%	Mapping diffuse features/point sources
PSF as function of radius out to 70% encircled energy	3%	Flux determination. Remove point sources in diffuse emission
PSF as function of azimuth out to 70% encircled energy over $11' \times 11'$	10%	Mapping diffuse extended features and jets

The high level calibration requirements translate into the following requirements that apply directly to focal plane calibration.

1. The uncertainty in position bias correction in the measurement of the X-ray interaction relative to a physical detector coordinate system shall be less than 100 μm anywhere on the active area. This pertains to the systematic part of the positioning due to detector distortions.

2. The Quantum Efficiency of each focal plane hybrid detector shall be determined to 5% accuracy in the 6–80 keV range.

3. The photopeak efficiency shall be determined to 3% accuracy in the 6–80 keV range.

4. The transparency of the `Be` entrance window shall be determined to 0.5% accuracy between 6 and 80 keV.

5. The focal plane/electronics system shall measure the absolute energy of an X-ray to better than 0.5 keV (3-σ) from 10 to 60 keV.

Apart from these five requirements for the Focal Plane Module (FPM), we also worked to verify the transparency of the optics thermal covers at low energies. The transparency data fold into the overall uncertainty of the optics throughput at low energies.

3.2 Detector Screening, Selection, and Calibration Steps

NuSTAR flight hybrids were made by the Space Radiation Laboratory (SRL) at Caltech, spanning the full range from design to testing and calibration. The life of hybrids begins with selecting the right ASIC and crystals. The manufacturer of `CdZnTe` (EI Detection & Imaging Systems, Saxonburg, Pennsylvania) provided us with IR diffraction images of the wafers, to select suitable uniform regions to be diced into NuSTAR `CdZnTe` crystals. These crystals were then taken to Brookhaven National Laboratory (BNL) for X-ray diffraction imaging. The diffraction images were examined to identify any crystal defects which could degrade charge transport properties of the detector. The best crystals which passed these inspections were selected for attaching anode and cathode contacts. A final selection step was to measure the bulk and surface conductivities as a proxy for leakage current. High

leakage crystals were rejected. In parallel, ASICs from ON semiconductors were tested for basic functioning. They were then subjected to "burn in"—an accelerated device aging test by heating at high temperature for one week. The ASICs were tested again and ones with low number of disfunctional pixels and no degradation through bakeout were selected as flight ASICs. The best CdZnTe crystals and the best ASICs were bonded to form candidate flight hybrids. At this stage, we commenced the selection and calibration of eight hybrids to be flown on board NuSTAR (Figure 3.2). Some selection steps were interspersed with calibration, as hybrids showing poor performance were demoted from "flight" to "backup" status.

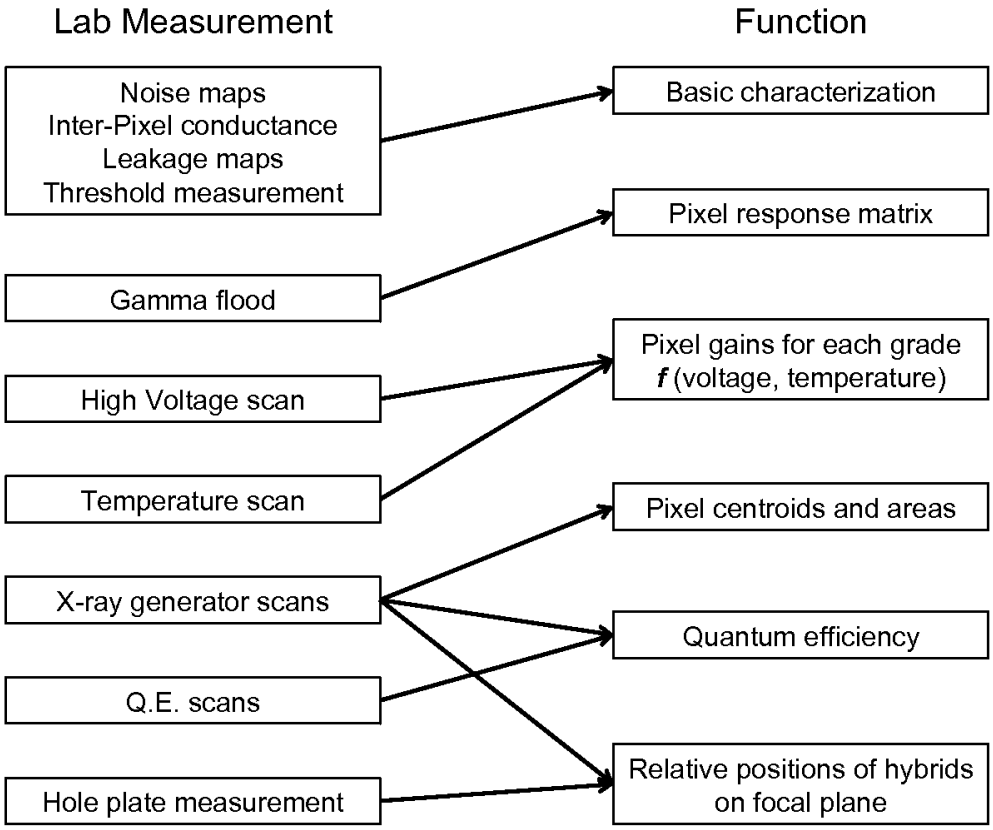

Figure 3.2. Overview of the calibration procedure. The left column lists various measurements undertaken in the laboratory. The right column lists the requirements and "measureables" for calibration. Calibration steps may be related to multiple requirements, and vice versa.

3.2.1 Hybrid Selection and Screening

The first screening step is to shine a radioactive source like ^{241}Am on a hybrid and generate an output spectrum. This allows to verify the functioning of the hybrid including noise performance, number of dead pixels, and approximate energy resolution. Next, we undertake more detailed characterization of the noise to make noise maps. We also measure the interpixel conductance (IPC) and reject any hybrids with high IPC values. To improve energy resolution, it is desirable to operate hybrids with higher values of potential difference between the anode and cathode. However, increasing the high voltage (HV) increases the leakage current in the pixel, and thus the baseline charge deposited in each sampling capacitor in a sampling interval. This, in turn, increases the probability of getting false triggers due to a voltage above the trigger threshold. We measure the leakage current for each hybrid to select its optimal operating HV. The measurement is repeated at various temperatures, to verify stability around the operating point. Based on these characteristics, we identify the few noisiest pixels in each hybrid, and disable them during regular operation.

Pixels are triggered when the charge deposited exceeds a certain threshold value. This threshold value is set by an external Digital-to-Analog Converter (DAC) on the motherboard. We want to set the threshold value as low as possible, to detect lower energy photons. However, this also increases the spurious noise triggers, decreasing the instrument live-time. Hence, we test various threshold values to determine the lowest possible setting where the noise contribution remains negligible, with less than ten noisy pixels disabled.

3.2.2 Pixel Response Calibration

As discussed in Section 2.5, we need to establish a channel to keV conversion for each pixel and grade combination. We calculate this mapping using X-ray line emission from the radioactive isotopes ^{57}Co, ^{241}Am, and ^{155}Eu (Figure 2.9). To obtain sufficient statistics to calculate these conversions, we undertake "γ flood" integrations for 48 hours for ^{241}Am and 24 hours each for the other two isotopes.

Several aspects of the functioning of the hybrids depend on extrinsic factors. The electronic noise and pixel gains vary with operating temperature. At higher temperatures, the leakage current in CdZnTe increases and can effectively saturate the readout. The ASICs do not function properly at very low temperatures. We take ^{241}Am spectra at varying

temperatures to measure these variations and determine the operating temperature. It was seen that the hybrids perform best at ∼5° C, well within the temperature range attainable in-orbit. Leakage current and pixel gains depend on the applied HV, too. Hence, we take ^{241}Am spectra at the operating temperature with different HV settings. It was found that the optimal HV is −400 V for four of the flight hybrids and −450 V for the other four. Data from these HV scans are also analyzed for measuring the $\mu\tau$ products for electrons and holes in CdZnTe, to be used in modeling the detector charge transport properties.

3.2.3 X-ray Pencil Beam Scan

Pixels in NuSTAR hybrids are formed the spacing anode pads and are not physically insulated from each other (Figure 2.4). From X-ray diffraction images, we know that the CdZnTe crystals have various defects which will deform the electric fields. Apart from these impurities, we also have to map out which regions of the hybrids preferentially give single or multiple pixel events. With this aim in mind, we scanned every hybrid with a fine X-ray pencil beam. From charge transport simulations, we expect that split pixel events will typically occur roughly in a hundred micron wide region near pixel boundaries. To effectively map this, we selected a beam size one-tenth the size of the 605 μm pixel. These scans are the first ever to probe the structure and functioning of CdZnTe detectors at such fine scales. The design, setup, and execution of these scans forms a large part of my thesis work, and will be discussed in detail in Sections 3.3 — 3.5.

3.2.4 Quantum Efficiency Measurement

The final step in calibration of the hybrids is measurement of the absolute quantum efficiency. The modus operandi for QE measurements is to take a well-calibrated radioactive source, and measure its total fluence using a NuSTAR flight hybrid. The ratio of the counts detected in the hybrid to the known source intensity is the QE. In practice, we measured the QE independently at various energies and for different regions of each hybrid. These measurements of average QE of regions of the hybrid are augmented by the X-ray scan data to calculate the absolute QE of each pixel. QE measurements are discussed in detail in Section 3.6.

3.3 The X-ray Generator Laboratory

I designed and implemented the X-ray Generator (XRG) Laboratory setup for undertaking the X-ray pencil beam scans and QE measurements. Later, we also adapted the setup for transparency measurements of the flight Be windows and optics thermal covers. Let us look at the essential details of the XRG lab to obtain context for the sections to follow.

3.3.1 Hardware Design

The primary hardware component of X-ray pencil beam scans is an X-ray generator with a collimator to produce the fine beam. For scanning, it is practical to translate the hybrids in front of a stationary X-ray beam. The enclosure for the hybrids should maintain operating conditions. External hardware provides power, data, and control signals. The same setup should allow replacement of the X-ray beam with a radioactive source for QE measurements.

The workhorse instrument is a 3 kW X-ray generator by Rigaku Corporation.[1] We use the XRG with a Molybdenum (Mo) tube, obtaining a Bremsstrahlung spectrum superposed with Mo K lines. The X-ray tube is housed in the XRG tower—an Al cylinder lined with lead on the outside to contain the intense radiation. A 12×4 mm aperture produces a divergent beam (opening angle $\sim 45°$). We collimate this beam down by using a pinhole at the end of a 43 cm beam tube (Figures 3.3, 3.4). Due to space restrictions, the beam tube has to be placed a short distance from the tower aperture. To contain any radiation that may leak from this space, we added an acrylic cylinder with lead sheets on the inside to contain all scattered radiation. A second layer of safety is provided by leaded glass panels with interlocks, which switch off the X-ray beam if opened. Lastly, the side of the enclosure which directly intercepts the beam has thick Al plates. The total radiation leak from the entire setup under operation is undetectable for our "low energy" configuration, and under 0.07 mR/hr for the "high energy" configuration.

The design goal is to obtain a beam of ~ 60 μm at the detectors. Space constraints and safety considerations dictate that the detector surface is at least a few centimeters from the pinhole. With the small desired spot size and relatively short beam length, beam divergence becomes a serious consideration. One way to control the beam size is to add multiple collimating pinholes along the beam path. However, this significantly decreases the source flux

[1] http://www.rigaku.com

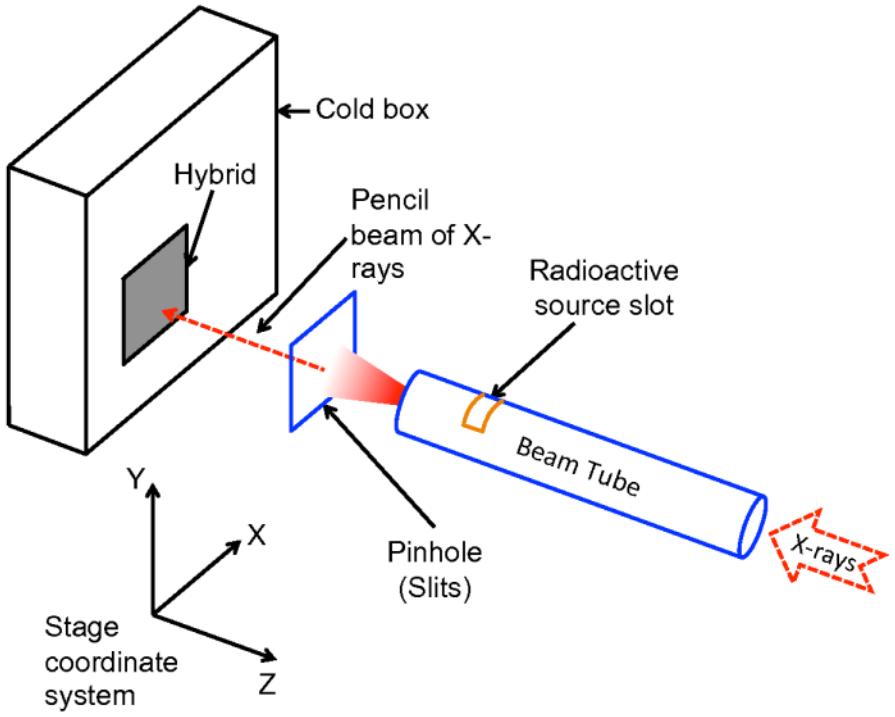

Figure 3.3. Schematic of XRG setup. A hybrid (gray) is mounted vertically in a cold box that can be translated on X-Y stages (not shown). The stage coordinate system is shown in the lower left. X-rays are generated by an X-ray tower on the right (not shown). The divergent X-ray beam travels along the $-Z$ direction through horizontal beam tube (blue) to a pair of slits forming a pinhole. The pinhole forms a mildly divergent pencil beam which is incident on the hybrid. For "QE scans," a radioactive source is inserted in the beam pipe, and the pinhole is replaced by a square mask. A photograph of the setup is shown in Figure 3.4.

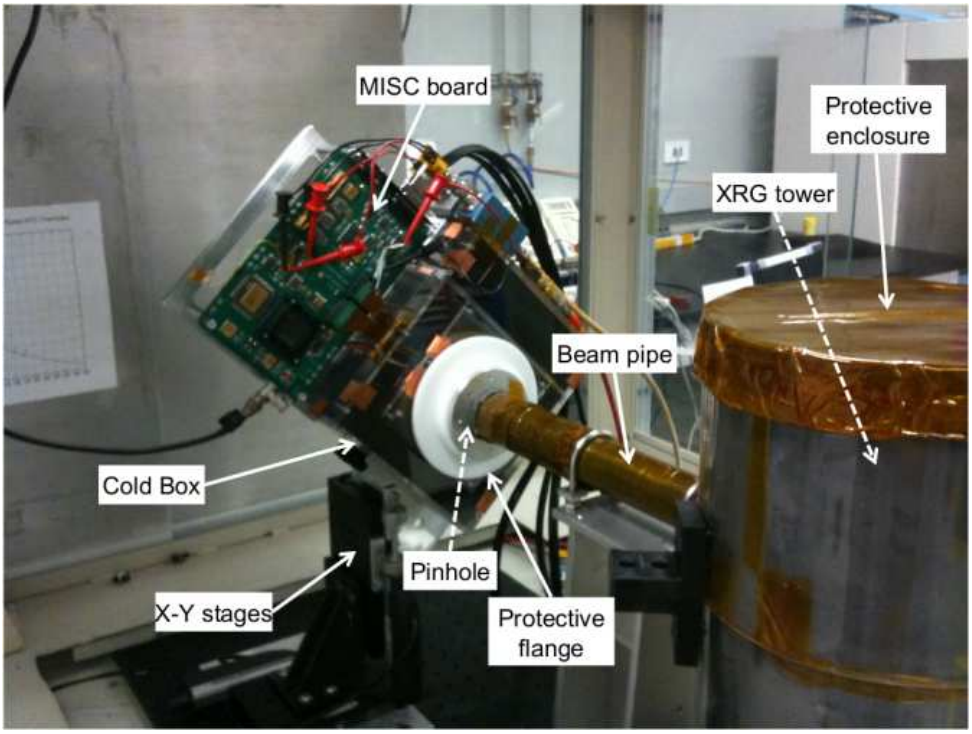

Figure 3.4. Photograph of XRG setup. X-rays are generated by an X-ray tower contained within a protective cylinder lined with lead (gray, right). X-rays travel through horizontal beam pipe to a pinhole concealed beneath the protective flange (white). Hybrids are mounted vertically in the controlled environment of the "cold box." The cold box is mounted on X-Y stages for translation. A MISC board with external connections is seen on the upper left of the cold box.

and makes alignment extremely difficult. Instead, we choose to account for the divergence in design by using a smaller pinhole and using the minimum practical pinhole–detector distance. This leads to a desired pinhole diameter of $\sim$40 μm, surrounded by material thick enough to block the intense X-ray beam. The pinhole needs to be elongated in one direction to compensate for the rectangular aperture of the X-ray tower. We accomplished this by using a pair of crossed slits, made from tinned lead. The slit widths were tweaked to the desired size under a microscope and the blades were then clamped down by screws. After multiple iterations, I achieved a slit size of 30×50 μm. Using a raytrace model, I calculated that the spot size on the detectors is 70×50 μm (FWHM, Figure 3.5).

We modify the same setup for QE scans. A slot cut in the X-ray beam tube can be opened to insert a radioactive source holder. The three calibration sources (^{57}Co, ^{241}Am,

^{155}Eu) were mounted in their respective holders throughout the calibration process, to minimize variations of experimental conditions. A pin on the source holder ensures accurate source positioning to better than a mil (25 μm). The fine slit is removed and replaced with a "QE mask": a sheet of tinned lead with a precisely milled square hole at the center. In this configuration, the radioactive source illuminates a 12×12 pixel grid on the hybrid.

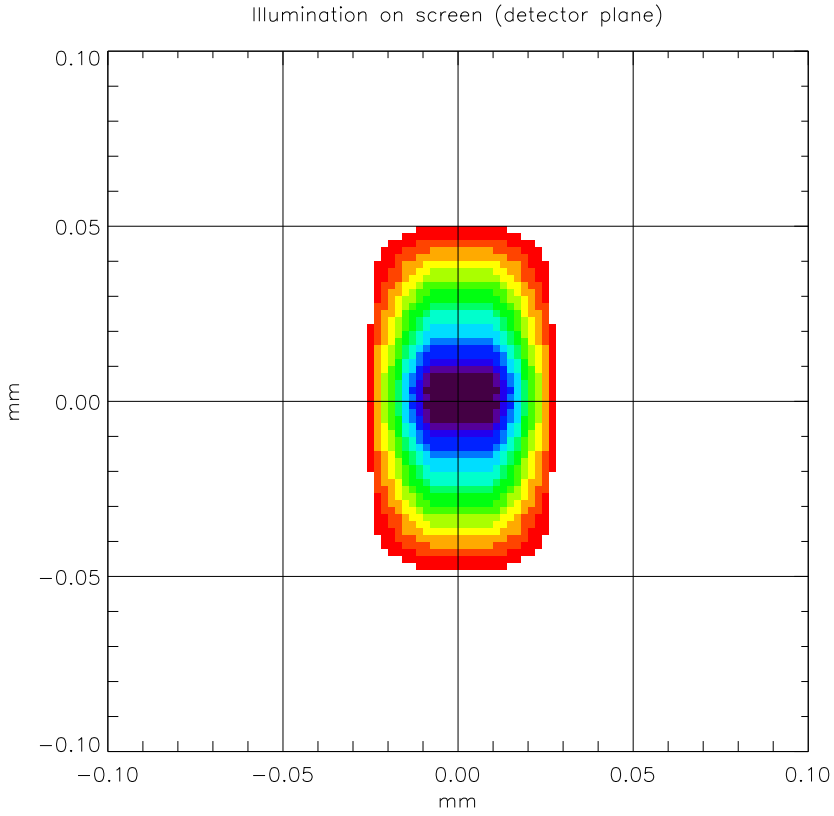

Figure 3.5. Simulated profile of the fine XRG beam on a detector. The beam is collimated by a 30×50 μm pinhole.

The hybrids are mounted on a motherboard screwed in vertically inside a "cold box" (Figure 3.4). X-rays are incident on the hybrid through a Mylar film. The box is cooled by pumping in cold, dry air from a forced air unit through an opening on the side. The box has 1/2" to 1" thick insulating foam on the inside to decouple it thermally from the surroundings. Air flowing directly onto the hybrid can excite microphonic vibrations in the detector, which result in increased electronic noise. To counter this problem, we have a diffuser which sends the cold air in through several small apertures such that no stream is

directly incident on the hybrid. The exit hole is diagonally opposite the entrance hole to ensure proper air circulation inside the cold box.

We use a pair of Newport LTA-HS translation stages to scan the cold box and the hybrids across the X-ray beam. These stages have an absolute accuracy of ± 7.5 μm and are positional repeatability of ± 1 μm. The 50 mm stage traverse leaves a few millimeter margin over the desired range for scanning all four hybrids mounted together on the motherboard. In practice, scheduling issues led to calibration of one detector at a time. The stages are controlled by a Newport ESP-300 stage controller, commanded by custom software on a PC (Section 3.3.2). The entire assembly is designed so that the mounting of the detector relative to the beam (including joints to motherboard, cold box, stage, optics plate) is repeatable to about a millimeter. The final position is tweaked by checking the beam position in software, and issuing an offset command to get the beam to an expected location. Hardware and software limits ensure that there is neither excess strain in connectors, nor any physical risk to flight hardware due to erroneous stage operation.

For reasons discussed later, the lab humidity is usually maintained at around 50%. When hybrids are cooled for testing, condensation develops on the outside of the cold box. We employed several measures to mitigate any risk of water seeping to the hybrid. First, the cold box is designed and mounted so that any liquid drip path completely bypasses the hybrids. Second, and more importantly, we decided to put the entire apparatus in a nitrogen environment in a purge box (Figure 3.6). Before cooling down the apparatus, we start the N_2 flow to purge out the vapour–bearing room air from the box. The purge box is designed so that opening and closing it is quick: this allows us to make minor modifications inside the box (like swapping radioactive sources) in a short duration and close the box again without any risk of getting condensation on the cold box.

A major concern in handling our hardware is electrostatic discharge (ESD). The potential difference in such discharges can be as high as kilovolts, and can potentially damage the electronic components. Even partial damage to any electronic components is a high risk, as the component may fail during the mission lifetime in orbit. We take several steps to mitigate the risk of ESD in the lab. All equipment are connected to a common ground to ensure that they are at the same potential. Ambient humidity is maintained at near 50% while handling all electronics, as dry air greatly increases the risk of ESD. Lastly, we

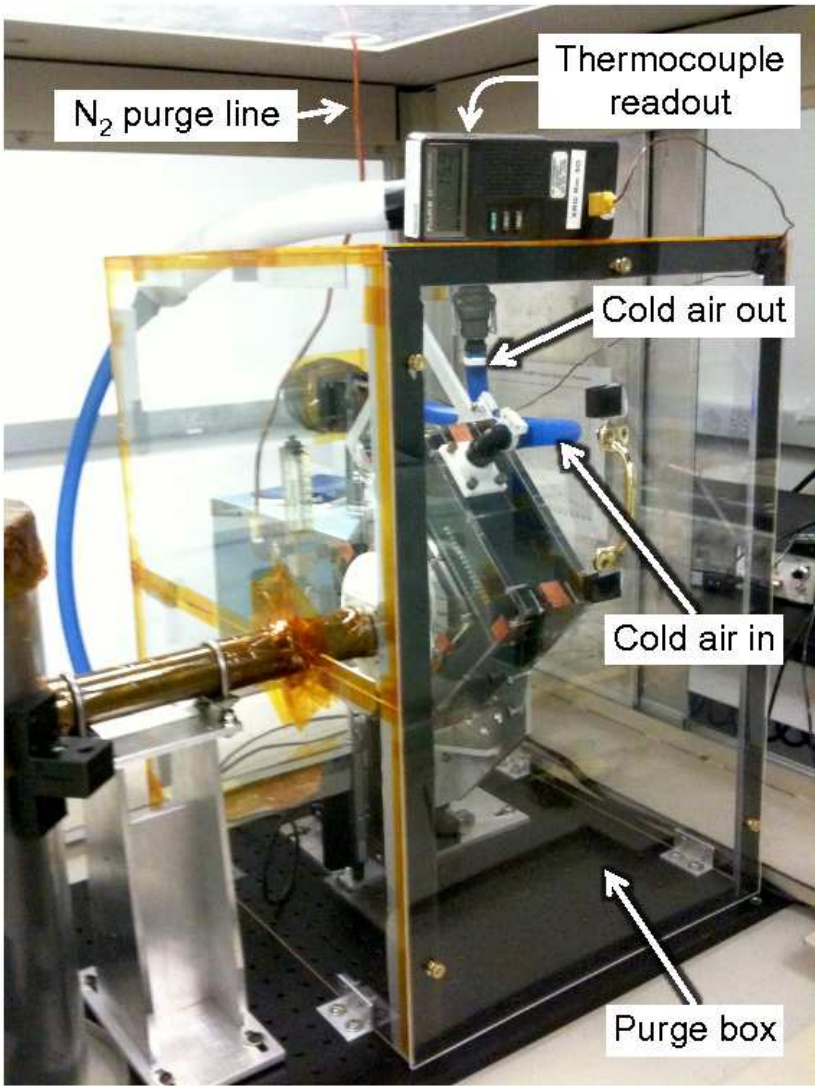

Figure 3.6. Cooling and purge systems for the XRG setup. Cold, dry air from a forced air unit (not seen) enters the cold box from the right and flows onto the hybrid through baffles for diffusing the air flow. Another air pipe leads the air out through the top of the enclosure. The transparent enclosure is the purge box. N_2 boiloff from a liquid nitrogen tank is fed into the box by a copper pipe (top). The gas diffuses out through spaces in the box, maintaining a dry environment inside.

take steps to avoid discharge spikes. Insulating surfaces are conducive for large buildup of charge, while conductive surfaces facilitate rapid discharge. To avoid both these cases, most lab surfaces are specially coated to be static dissipative: such surfaces dissipate charge at a low enough rate to not risk any hardware damage. All lab operators are trained in ESD

safety precautions as per JPL guidelines.

3.3.2 Control Software

The X-ray generator setup is controller through custom software. The basic requirements of the software were

1. Command interfaces to the ESP300 stage controller and the NuSTAR ASIC,
2. Automation of XRG and QE scans,
3. Combine stage and ASIC data into a flight-like format which can be processed by existing analysis software,
4. Ability to remotely control and monitor operation,
5. Complete and comprehensive logging of all hardware and user interaction, even in case of crashes,
6. Ability to manually override any steps if required,
7. Flexibility to execute test cases.

To take advantage of existing code and availability of drivers, we decided to use Microsoft Windows to interface with the hardware. To execute the calibration scans, I developed a graphical user interface (GUI) in `VC++` (Figure 3.7). This custom `StageGUI` software interfaces with the hybrid as well as the stage controller. The hybrid interface utilizes two `RS422` ports. First, the MISC is initialized and booted over the command port. The bidirectional port is then used for sending commands in the `forth` language and monitoring responses. The other port is the unidirectional data port, which is continuously monitored for event data. For test and debugging purposes, a `WinForth` terminal on the PC can be used for interfacing with the hardware. The ESP300 stage controller provides a fully functional command interface for controlling any connected translation stages. We use the `RS232` serial interface to the controller. To ensure repeatability of scans, `stageGUI` initializes all basic parameters of the stages, including units, software limits, velocities, and accelerations.

A typical XRG or QE scan begins with a default bootup procedure, followed by interactively commanding the hybrid to establish stable working conditions. The operator then

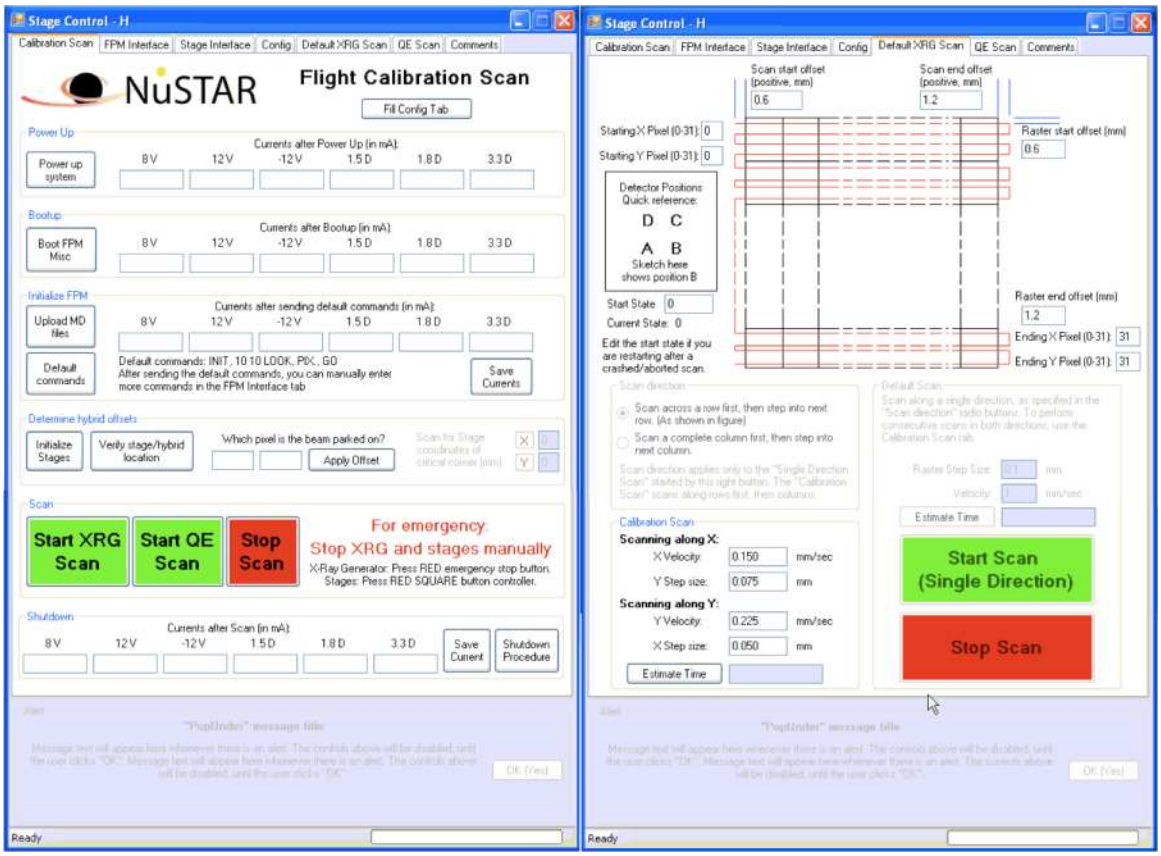

Figure 3.7. `StageGUI` control software. The principle "Calibration Scan" tab (left screenshot) guides a user through powering up the hardware and establishing stable operating conditions. Individual tabs allow direct command access to the ESP300 stage controller or to the hybrid. Other tabs are used to set up the XRG scan (right screenshot) or QE scans. The config and comments tabs are used for logging information.

sets the parameters of the scan to define the movement pattern for stages. `StageGUI` controls the movement of the hybrid by commanding ESP300 appropriately. Event data from the hybrid is recorded as a continuous stream. At predefined intervals, `StageGUI` queries the stage position and adds a stage position packet to the data stream. The stage packets follow the NuSTAR data format, so that any existing analysis software simply ignore these packets and are still able to process data.

All user interactions and automated commands are logged to the screen and written directly to disc without buffering. This ensures traceability of crashes and issues. Debug modes can be invoked to override the default command sequence. Toggling of debug modes is logged as well. Remote monitoring is achieved by using the `Teamviewer` software, with re-

dundant access is obtained by using the `logmein` service.[2] Data are periodically transferred to `sarasvarti`, the main NuSTAR server.

3.4 Calibrating the Setup

We undertook extensive characterization of the setup to qualify it for calibrating NuSTAR flight hardware. For XRG scans, the primary requirements are measurement of the pencil beam profile and verifying that the XRG flux is constant over the duration of a scan. For the QE setup, we had to measure the fluence of each source with high accuracy. Here I describe how I accomplished each of these goals. We also tested the reproducibility of various quantities calculated from scans. These tests are discussed later, with the analysis of respective scans.

3.4.1 Beam Shape

As seen in the raytrace (Figure 3.5), we expect the pencil beam to be symmetric in both X and Y directions. We measured the X and Y profiles of the beam with a knife edge scan. We place a detector at some distance from the slit such that it intercepts all the X-rays coming from the slit, then move a knife edge to progressively occult greater fractions of the beam, and measure after each step of the knife edge. The difference in count rates between successive steps is the count rate in the obscured part of the beam. We used an Amptek `Si` detector with a circular input collimator of 2.38 mm diameter. We know from raytrace modeling that this detector will intercept the full X-ray beam even at several inches from the slits. Since we want to measure the beam profile at the fiducial `CdZnTe` surface, the knife edge is kept in that plane, while the `Si` detector is mounted further away from the slit. We acquired data by stepping the knife edge by small amounts ($\sim$10 μm) between integrations. We measured the beam FWHM to be $\approx$50 μm in X and $\approx$70μm in the Y direction (Figure 3.8). Consistent results were obtained on repeating the knife edge scan after several months, after calibration of flight hybrids.

[2] http://www.logmein.com

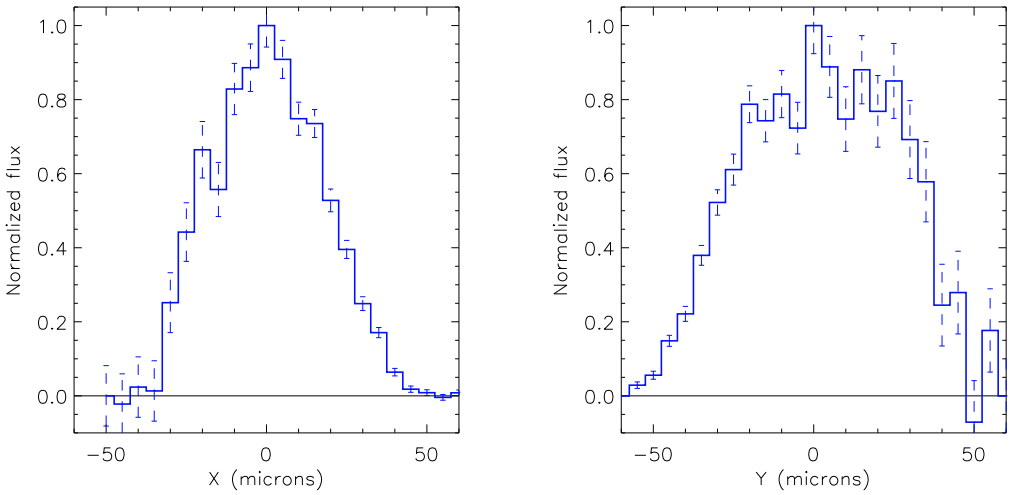

Figure 3.8. XRG beam profile with a knife edge scan in the X (left panel) and Y directions (right panel). The blue lines show the differential count rate measured by moving the knife edge in steps of 5 μm, normalized such that the peak response is unity. The dashed error bars show Poisson uncertainties in fluxes. The physical coordinates are set to be 0 at the peak intensity of the beam. The measured beam FWHM (Δ) from multiple knife edge scans is ΔX $\approx$50 μmand ΔY $\approx$70 μm.

3.4.2 Rate Stability

The rate stability of the XRG was tested in two ways: first, with a `Si` detector and a scalar, and then with NuSTAR detectors.

I set up the X-ray generator (XRG) with a 50 $\times$ 70 μm slit, which generates a spot size of 100 $\times$ 100 μm at the detector. I used a `Mo` tube, operated at 45 kV, 20 mA. Data were acquired using the Amptex `Si` detector and a scalar. The background rate for this detector is negligible: $\sim$0.03 counts/s. I aligned the `Si` detector to the XRG beam using the MCA for quick readout. The detector position was adjusted to achieve maximum count rate. Then I swapped the MCA with the scalar. The measurements were done by manually starting and stopping the scalar acquisition as per a stopwatch. The time recorded on the stopwatch ($\simeq$10 s) was used to calculate count rates. The RMS scatter in the time intervals is 0.1 s. I took 50 readings for the XRG, at a count rate of about 400 counts per second. For comparison, I also obtained 20 readings with an ^{241}`Am` source, with distance adjusted to get a similar count rate.

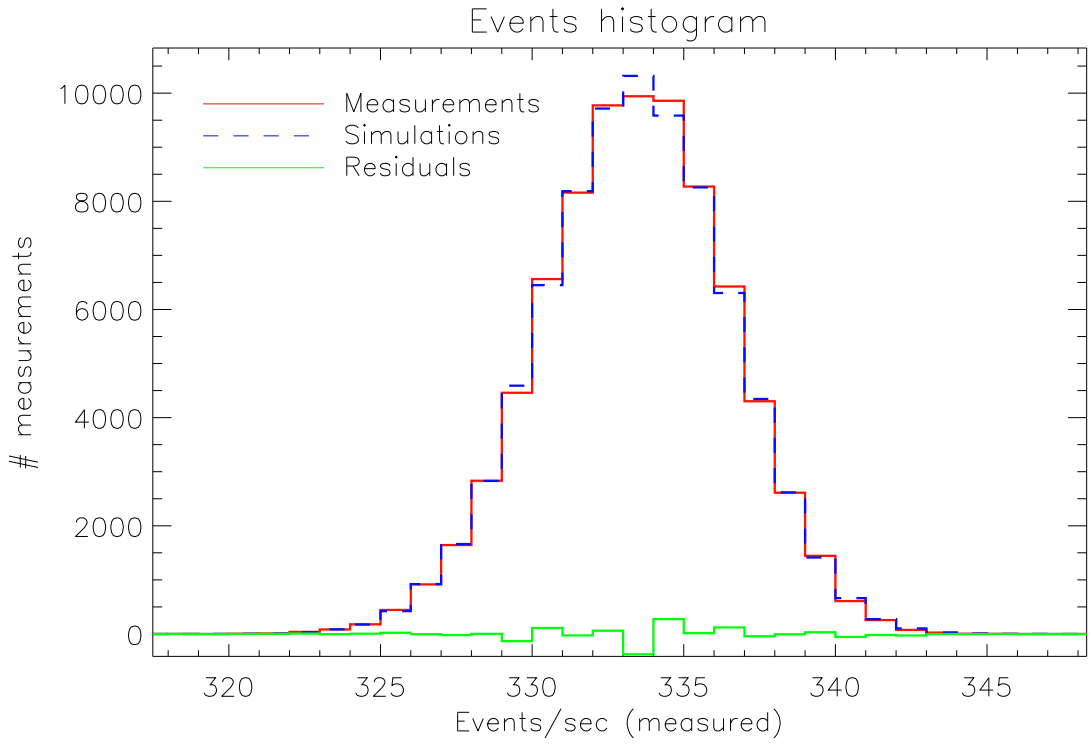

Figure 3.9. XRG stability measurements. The red curve is a histogram of counts per second obtained in a 22 hour integration. The mean of the histogram is sensitive to the input count rate, while the width depends on the dead-time per event. The dashed blue histogram shows a simulated distribution adjusted for the input count rate, using 2.5 ms dead-time per event. The residuals (green histogram) demonstrate the good quality of the fit.

The measured counts for the ^{241}Am have a mean of 440 counts/s. The scatter in readings is 6.6 counts/s—consistent with a Poisson distribution. This test shows that the Si detector and scalar combination gives a reliable measurement of the count rate. For the XRG, the mean count rate is 412 counts/s, with a standard deviation of 6.4 counts/s. This is consistent with the expected scatter for a Poisson distribution.

Next, I conducted a stability measurement using the NuSTAR detectors themselves. I set up the XRG at 20 kV, 2 mA, and placed H78 in a the cold box to intercept the beam. The stages were manually adjusted so that the beam was placed close to the center of a pixel. I measured a count rate of about 333 counts/s. Data were acquired for ∼22 h, yielding about 79,000 one-second count rate measurements. It was observed that the count measured by the detector was constant over the entire run. Due to the dead-time interval

associated with reading out each event, the count-rate distribution is a modified Poisson process (Figure 3.9). The observed data are in excellent agreement with a simulated count rate distribution for an incident beam with constant flux. The mean of this distribution is sensitive to the total count rate, while the width depends on the dead-time per event. Using this data set, I verified that the dead-time per event is 2.50 ms.

3.4.3 Radioactive Source Fluence

As explained in Section 3.2.4, the quantum efficiency measurements consist of shining a radioactive source with a known count rate on a part of the detector, and calculating the QE from the measured count rate. A prerequisite for this is knowing the source flux well. We accomplished this by measuring the source count rate with good statistics, using a Ge detector. We have a detailed model for the response of the Ge detector from previous work. We placed each radioactive source in turn in the beam tube with the QE mask, and placed it such that the distance from the Ge detector was same as the distance from the CZT detector during calibrations. The calibration Mylar window covering the cold box was also added in the beam path. In this configuration, the Ge detector intercepts the entire beam coming from the QE mask. During calibration, the source and detector were both inside the purge box, in a nitrogen environment. In the ≈2.5 in gap between the source and detector, air absorbs about 15% radiation at 6 keV, while N_2 absorbs only about 12%: a significant difference. Ambient humidity further increases the absorption in air. So, we placed the entire setup in a nitrogen bag. We then took long integrations to beat down Poission noise, and measured source fluxes with high precision. The count rate of the ^{55}Fe (∼40,000 counts/s) is too high for the Ge readout electronics. We could not revert to the Amptex Si detector since its active area there is too small to intercept the full beam. Hence, we decided to insert an attenuator to reduce the count rate on Ge to about 180 counts/s. In turn, we would calibrate the attenuator itself using the Si detector, by simply taking an I/I_0 pair of measurements with and without the attenuator respectively. With a combination of these steps, we calculated the final fluence of the 3 calibration sources through the QE mask to be ≈150 counts/sfor ^{155}Eu, ≈60 counts/sfor ^{241}Am, and ≈30,000 counts/sfor ^{55}Fe. The uncertainties in these measurements were propagated through to the uncertainty in-flight detector quantum efficiency measurements.

3.5 Pixel Centroids and Areas

We use X-ray generator scans to measure the spatial response of hybrids to X-rays and calculate the centroid and area of each pixel. I describe the scan configuration and procedures in Section 3.5.1, followed by data analysis and results in Section 3.5.2.

3.5.1 Procedure

In the XRG configuration, we mount the fine slit (30×50 μm) in front of the beamline. A hybrid is mounted in the cold box on a flow bench. We mount the cold box on the translation stages and commence the cooldown procedure. The operators follow a hardcopy checklist throughout this process. When the hybrid stabilizes at operation conditions, we check the position of the X-ray beam and recenter it as needed. Throughout our calibrations, we found that the absolute position of hybrids was repeatable to about a millimeter.

We undertake two types of scans: a Low Voltage (LV) scan and a High Voltage (HV) scan (Table 3.2). For the LV scan, we operate the XRG at 20 kV, generating a relatively "soft" spectrum. The e-folding path of a 15 keV photon in `CdZnTe` is merely 36 μm, so most of the photon interactions occur very close to the cathode. The charge cloud moves through the full depth of the `CdZnTe` crystal, so LV scan results reflect charge transport properties of the entire detector. Higher energy photons penetrate deeper into `CdZnTe`. The electron cloud generated by such an interaction will be unaffected by any crystal defects close to the cathode. To study this effect, we repeat the scans in HV mode with the XRG set to 60 kV (Figure 3.10). To avoid being dominated by the LV counts, we add a 2.3 mm `Al` slab in the beam path which absorbs the low energy component.

A typical scan consists of a full raster across the detector, once across rows and once across columns. The beam is moved across the full detector with some margin so that it definitely crosses over the edge of the detector. We call this the scan direction. Then we move it sideways (raster direction) by a step equal to the beam size in that direction, and then move it back over the detector to the other side (Figure 3.11). Such a scan is very effective in determining pixel boundaries perpendicular to the scan direction. In order to complete the mapping of pixels, we repeat the scan with raster and scan directions switched. Based on exact scan settings, we get ten to fifteen thousand counts in each pixel.

The NuSTAR requirement *L4-FPE-65* states, "The uncertainty in the position bias

Table 3.2. X-ray generator settings for hybrid scans

Mode	Voltage	Current	Incident Count Rate	Measured Count Rate
	kV	mA	counts s^{-1}	counts s^{-1}
LV	20	2	≈2000	≈330
HV[a]	60	2	≈10000[b]	≈385

[a]In HV mode, a 2.3 mm thick Al plate was added as a "filter" to decrease the total count rate by preferentially blocking lower energy photons.

[b]The beam had broad wings in HV mode, so only about one-fourth of the photons actually hit the target pixel, other photons were detected all over the detector.

correction in the measurement of the X-ray interaction relative to a physical detector coordinate system shall be less than 100 microns anywhere on the active area." This can be broken down into two sub-requirements: first, determining the centroids of each pixel on a hybrid, and second, measuring the relative positions of all detectors on the focal plane. The combined uncertainty from these two steps should be less than one hundred microns.

For planning the XRG scans, I carried out extensive simulations to determine the number of counts required per pixel, to attain the desired centroiding accuracy. I found that we can easily get this with as low as 360 counts per pixel, the centroid of pixels is determined to better than 8 μm (1-σ). We also need to map pixel boundaries reliably to measure the areas of pixels, as discussed later in Section 3.6. This places more stringent requirements on scans: the mean spacing between photon hits in a single pass of the X-ray beam should be $\sim$1 μm. Since the mean output count rate is 350–390 counts/s, this translates to a scan rate of 400μm s^{-1}, or about 8 hours per scan. For scheduling convenience, we extended the scan duration to 11 hours, such that the total duration of the start up procedure, LV scan, HV scan, and shutdown procedure is 24 hours.

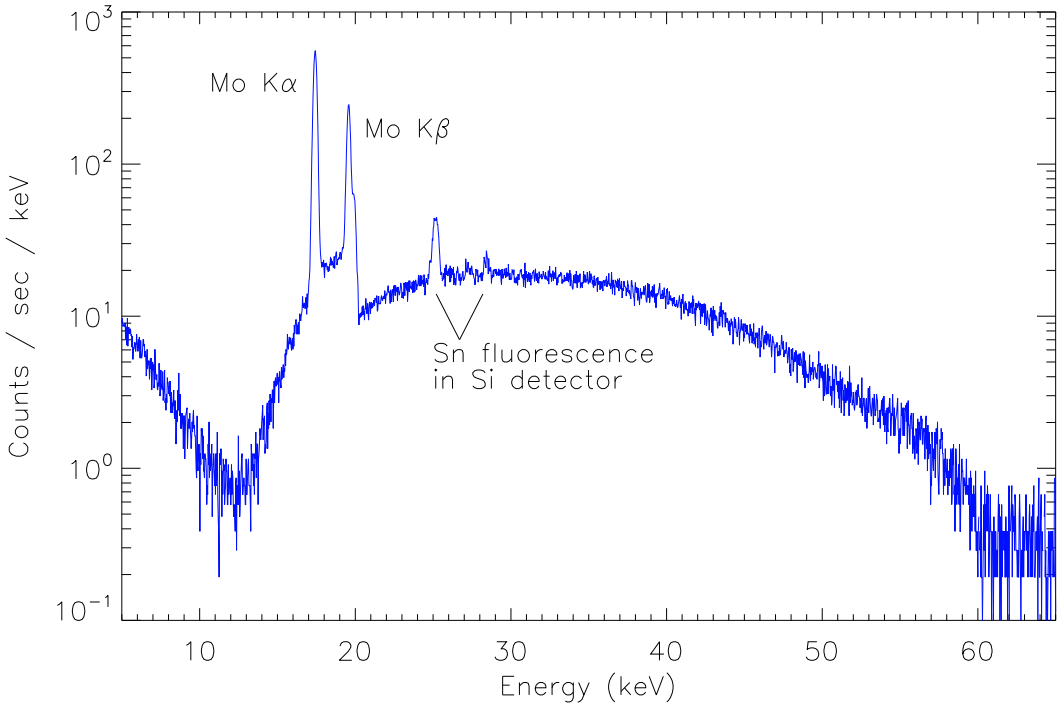

Figure 3.10. XRG spectrum in HV mode. The XRG was set at 60 kV, with a `Mo` target, and the spectrum was measured with a `Si` detector with a `Cu` + `Sn` collimator. The resultant spectrum is Bremsstrahlung superimposed with `Mo` Kα (17.4 keV), Kβ (19.6 keV), and the `Mo` K-edge ($\sim$20 keV). To reduce the count rate, we added a 2.3 mm thick `Al` filter in the beam path. This preferentially absorbs the low energy photons, giving the dropoff around 15 keV.

After completing every scan, we ran several tests to verify integrity of the data. Parts of this work were completed as the SURF[3] project of Nancy Wu. The first check was to plot all stage positions to ensure coverage of the entire detector. Next, we checked the number of raw stage data packets in each pass of the stage over the detector and the duration of each pass took, looking for outliers. Nancy visually examined zoomed–in plots of each pass to verify that the translation stages were not stuck in any part of the scan. The stage hardware was used with only a small margin under the maximum load limits, so occasional malfunctions were detected in data. In only a few cases, we had to rerun scans due to hardware issues. In hindsight, we would have designed the setup with a higher safety

[3]Caltech Summer Undergraduate Research Fellowship, http://surf.caltech.edu/.

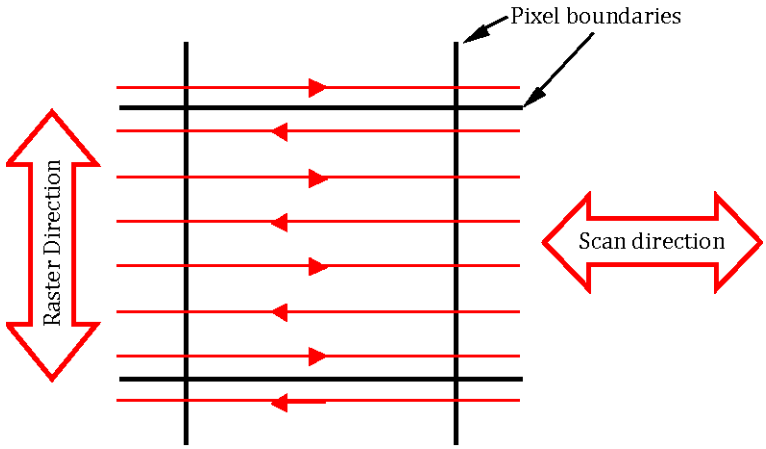

Figure 3.11. XRG scan procedure. The stages drive the hybrid so that the X-ray beam rasters over all pixels. Shown here, the beam traverses a pixel in the scan direction, then is stepped over by one beam width in the raster direction and traverses the pixel in the other direction. After completing such a scan over the entire detector, the scan and raster directions are swapped and the full scan is repeated.

margin, and compensated some of the stage loading by a pulley mechanism.

3.5.2 Analysis and Results

Scan data recorded in a flight-like binary format are transferred to the NuSTAR workhorse linux server "`sarasvarti`," where the files are converted to `fits`. All my analysis codes are written in `IDL`[4] and placed under version control on a `SVN` server.

The first analysis step is to calculate pixel centroids in stage coordinates. For events corresponding to every (pixel, grade) combination, we want to calculate the centroid of that area of the detector which generates such events. The net distribution of photons on the hybrid over a complete scan is uniform. So the area centroids simply the mean position of all photons generating the particular (pixel, grade) triggers. For LV scans, the beam is well contained within a narrow 50×70 μm spot, so the location of the translation stages at the time of the event trigger is a good proxy actual photon interaction position. This average of stage positions for all events forms the first estimate of the centroid. This position is iteratively refined by rejecting any events outside a 5-pixel-wide box centered on the current centroid estimate. This process is repeated until the centroid estimate shifts by less than

[4] http://www.exelisvis.com/idl/

15 μm in an iteration, or up to 5 iterations. Centroid calculations for HV scans are a bit more involved, as only about one-fourth of all photons are in the core of the wing, with three-fourths being distributed in very broad wings extending beyond the hybrid. As a result, the mean position of all photon hits is always close to the center of the hybrid. To surpass this hurdle, we use LV centroids as the starting estimate. As before we select photons within a 5-pixel-wide box around this start estimate. Most of the photons in such a box are from the core of the beam, and the $\sim$2% contribution from the wings can be ignored. The HV centroids are then iteratively refined as before.

The acid test for reliability of data is repeatability. I ran two complete LV calibration scans for H78, and analyzed the data sets independently to calculate centroids for each pixel. Comparing the results, we see that there is a small systematic offset between the centroids calculated from both scans: $\Delta X = 44$ μm and $\Delta Y = 2$ μm (Figure 3.12). After correcting for this offset, the scatter between the centroids calculated from both the runs were $\sigma_x = 11$ μm and $\sigma_Y = 8$ μm, comfortably smaller than the calibration requirements for NuSTAR.

Next, we use XRG scan data to calculate the boundaries and areas of individual pixels. The boundary mapping algorithm, developed as a part of Nancy Wu's SURF project, is as follows: the XRG scans are first split into individual passes over the detector. A typical flight calibration scan consists of about 400 passes in the Y direction and 300 passes in the X direction. For each of these passes, we assign events to the pixels with highest energy, independent of event grade. The boundary between two pixels is defined as the point where photons equally likely to trigger either pixel. XRG scan passes along the X direction are sensitive only to boundaries between pixel rows, while column boundaries are mapped from passes along the Y direction. The boundary of pixel (C, R) is calculated as the intersection of the column C and row R using the `IDL inside`[5] routine. Areas are calculated for each pixel and uploaded to the `SVN` server.

3.6 Quantum Efficiency Measurements

Measurement of absolute QE of pixels is a two-step process: determining the "Bulk QE" of a part of the detector using radioactive sources, followed by measuring "relative QE" of

[5] http://www.idlcoyote.com/tips/point_in_polygon.html

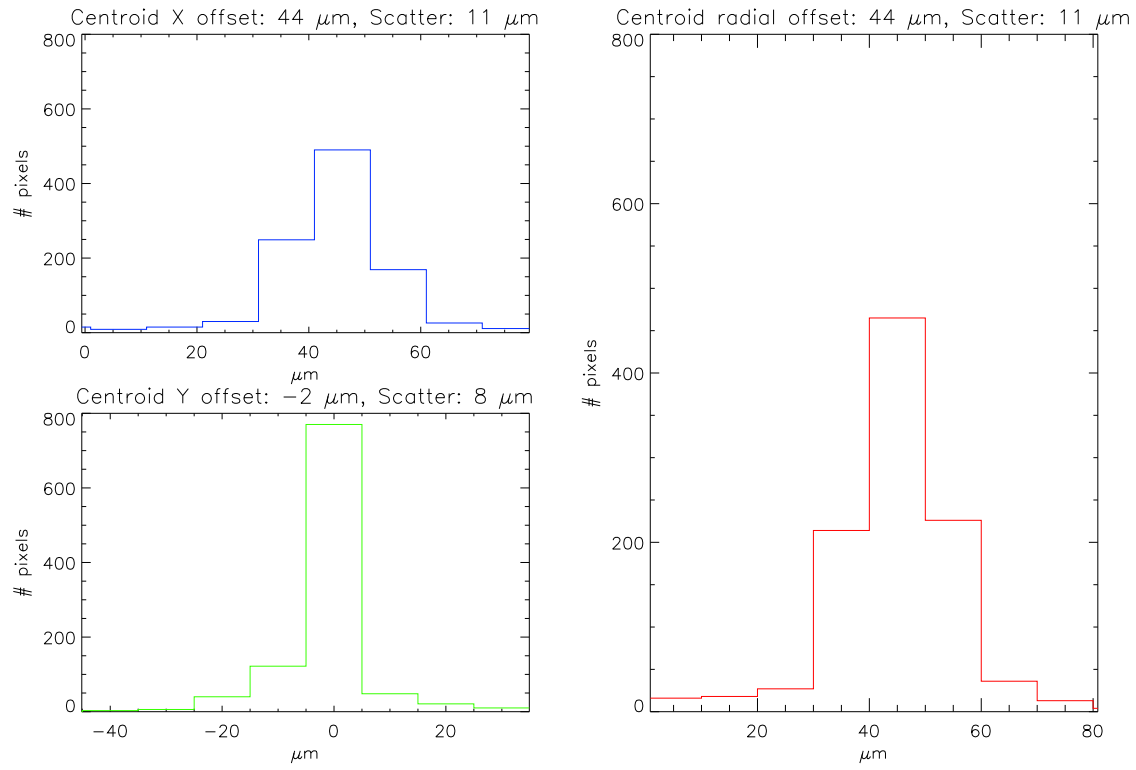

Figure 3.12. Comparison between centroids measured with two consecutive XRG LV scans for H78. The offsets were 44 μm in X and 2 μm in the Y direction. After correcting for this offset, the scatter between the centroids calculated from both the runs were 11 μm in the X direction and 8 μm in the Y direction.

various pixels from XRG scans.

3.6.1 Procedure

Absolute QE measurements were conducted with QE scans. We make minor modifications to the XRG scan setup: a well-calibrated radioactive source is inserted in the XRG beam tube and the fine slit is replaced by a QE mask (Section 3.3.1). This configuration is designed to illuminate a 12×12 region of the hybrid. In contrast to the continuous scanning procedure for XRG scans, the hybrid is parked at a single location for a "dwell" spanning 25–45 min depending on the radioactive source used. These durations are selected such that each dwell has $\gtrsim10^5$ counts, decreasing the uncertainty from Poisson statistics to well under a percent. After each dwell, the `StageGUI` software moves the hybrid over by half a mask size and

commences the next integration. Initial flight hybrid calibration scans consisted of a 6×6 grid of dwells. For dwells on the outer boundary of this grid, part of the source flux was incident beyond the active area of the hybrid, which rendered them less useful for absolute QE determination. For later calibration scans we narrowed down to a 4×4 grid of dwells, where all the source radiation was incident on an active part of the hybrid.

3.6.2 Analysis and Results

For the "Bulk QE" measurement, we split the scan data into individual dwells of the QE scan. Each dwell probes a different region of the hybrid. The data were reduced via standard NuSTAR pipelines to form spectra. We identified regions containing the photopeak and any tailing from a given line and added up all the counts in those regions to get count rates. The absolute QE is the ratio of the livetime corrected count rate for a hybrid to the total expected count rate from the radioactive source. For NuSTAR flight hybrids, the absolute QE is ∼98% in a significant part of the energy range of interest (Figure 3.13). QE values for different regions of the detector are constant within measurement errors.

To calculate absolute QE for individual pixels, we couple this data with "relative QE" measurements from XRG scans. While we have not calibrated the absolute flux of the XRG beam, we have verified that it is extremely stable over timescales of calibration scans (Section 3.4.2). Thus, any pixel-to-pixel variation in count rates in a XRG scan is indicative of the relative QE of pixels in that energy range. In particular, when the beam is near the center of some pixel, that pixel should detect all the counts from the beam, with no loss due to charge sharing or split pixel events. For each pixel, I extract counts from a 200×225 μm box around its grade 0 centroid (Section 3.5.2). Then I obtain the count rate by dividing by the hybrid livetime. A subtle but important effect arises from event triggers in other pixels. The data packet for each includes the livetime prior to the event. While events in other pixels should not be counted for measuring the count rate in the pixel of interest, we still have to add up the "prior" livetime from those events in the total livetime. The count rate is given by

$$\begin{aligned} \text{Count Rate} &= \frac{\text{Number of events in pixel of interest}}{\text{Total livetime of hybrid during the pass}} \\ &= \frac{\text{Number of events in pixel of interest}}{\Sigma\,(\textit{Prior} \text{ time of events in ALL pixels during that pass})}. \end{aligned} \tag{3.1}$$

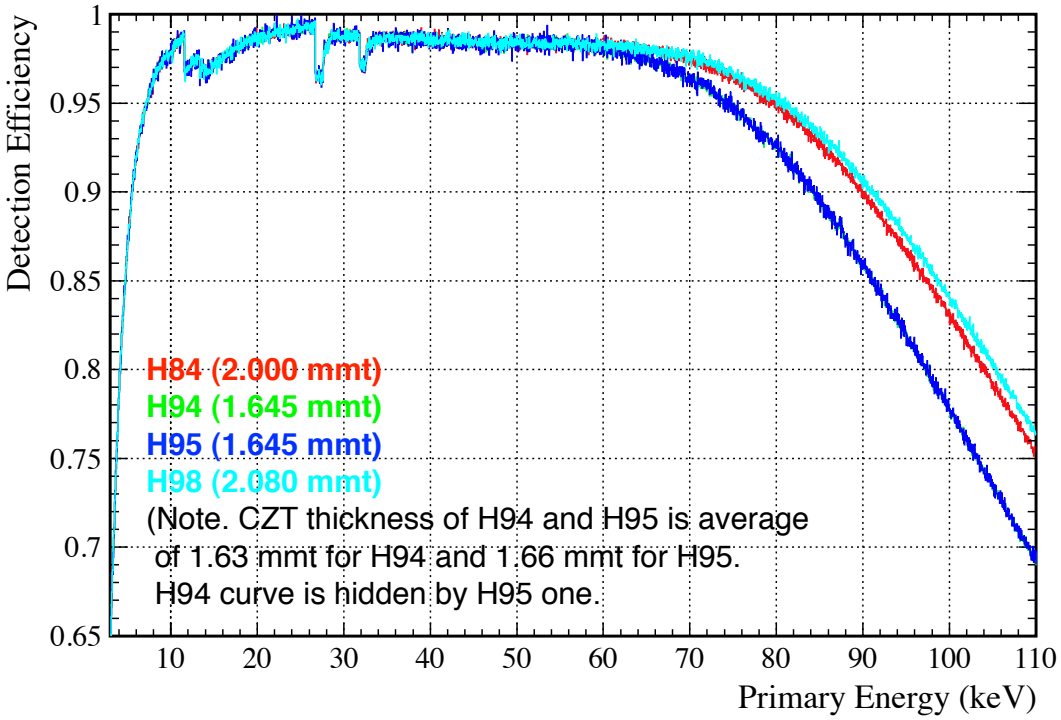

Figure 3.13. Absolute QE measurements for the four NuSTAR FPM-A hybrids. The QE is close to 98% over a significant part of the NuSTAR energy range. Plot courtesy Takao Kitaguchi.

The normalized distribution of these count rates gives us the relative QE of pixels (Figure 3.14).

In default XRG LV calibration scans, typical pixels record between 1000 and 2000 counts in the central extraction region. Thus, even for a detector with uniform QE for all pixels, we expect a ∼3% scatter in the measured values of QE. As in Section 3.5.2, we tested the repeatability of relative QE measurements in laboratory data. I calculated relative QE for all pixels H78 pixels independently from two scans. Comparing the two sets of measurements, I found no evidence for statistically significant variations in QE among pixels. This is consistent with the observation that the bulk QE for various regions of the detector is constant within measurement uncertainties.

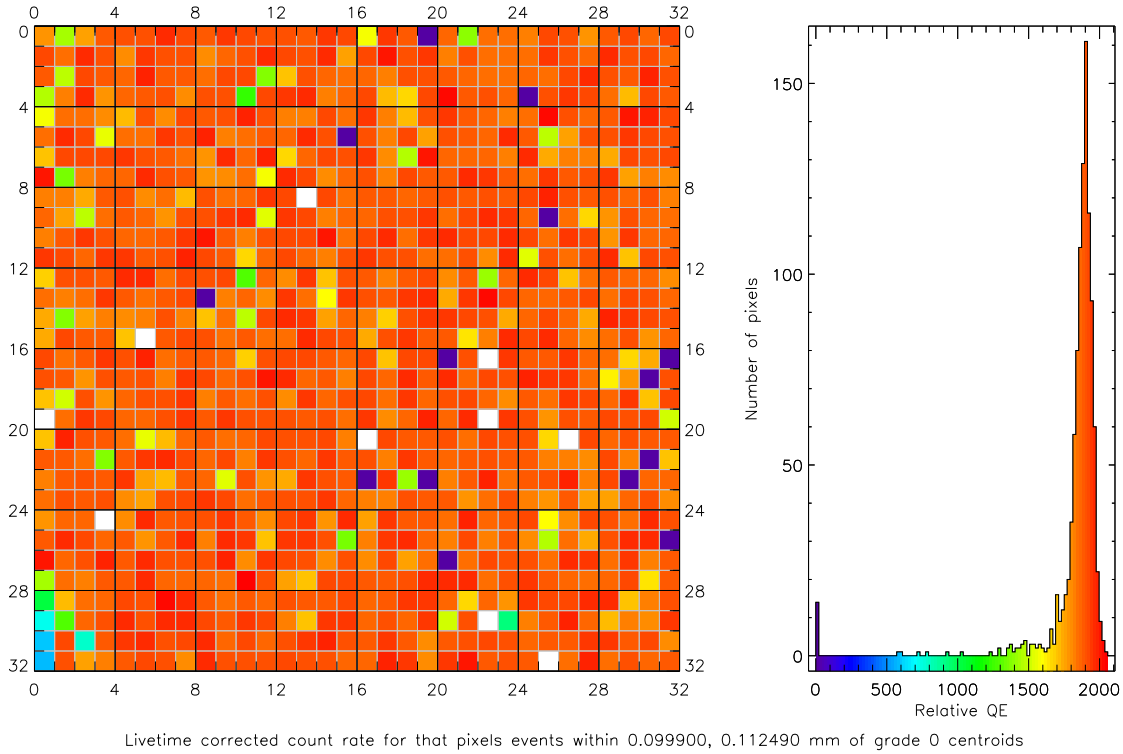

Figure 3.14. Relative QE measurements for H82. The color scale and histogram denote the count rate in the centers of pixels measured in XRG LV scans, which is proportional to the pixel QE. Apart from the low QE pixels in the lower left, the scatter is within that expected from Poisson noise.

3.7 Transparency

As discussed at the start of this Chapter, we adapted the XRG lab setup to measure transparency of two components of NuSTAR: Be windows and optics thermal covers.

3.7.1 Beryllium Windows

The NuSTAR focal plane modules have Be windows in the photon path, to block off low energy photons (Figure 3.1). This is important as even photons with energies lower than the pixel trigger thresholds can increase the background noise. In extreme cases, a high flux of X-rays can slightly lower the gain of the detectors. The aim of laboratory calibrations was to measure the attenuation of Be windows as a function of energy and position on the ∼3 inch diameter window.

To measure attenuation, we set up a radioactive source and a detector and measure

the source flux (I_0) in some X-ray line. Then we insert the Be window between them and measure the attenuated line flux (I). The ratio I/I_0 gives the attenuation at that energy. We repeat this procedure using radioactive lines at various energies. The attenuation of the window depends on its thickness and composition. We can calculate the expected attenuation curve based on composition information provided by the vendor (Table 3.3). Then, we fit the curve to data with thickness as the only free parameter.

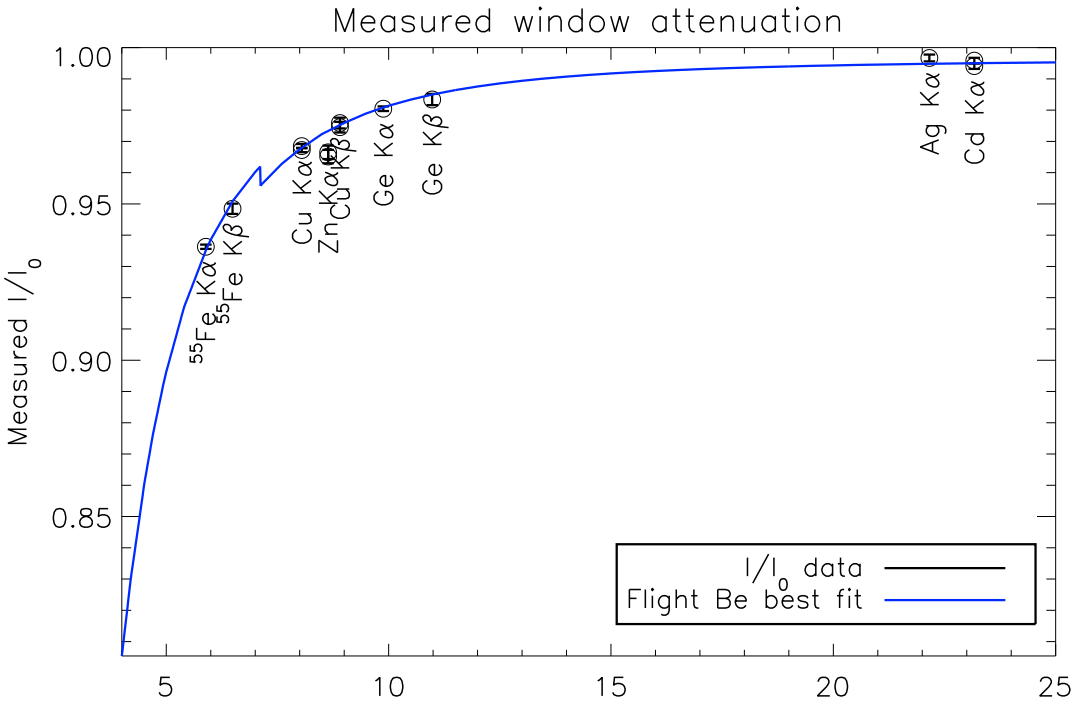

Figure 3.15. Best-fit attenuation curve for Be, using the composition from Table 3.3 and data from Table 3.4. We see that the vendor-specified composition gives a good fit to data.

The attenuation varies strongly with energy in the low energy (3–10 keV) range. At higher energies, the attenuation is lower and varies less strongly with energy—so this energy range can be sampled sparsely. We use the ^{55}Fe Kα and Kβ lines as the lowest energy probes. For intermediate energies, we use fluorescence lines from various materials irradiated by the XRG (Table 3.4). We modified the XRG setup to mount a target at 45° to the X-ray beam and placed the Amptek Si detector to intercept fluorescent X-rays. The observed spectrum consists of strong fluorescence lines superposed on a relatively weak compton scattered XRG spectrum.

Table 3.3. Be window composition

Element/Compound	Fraction by mass[a]
Be	0.99145
BeO	0.0070
Al	0.0004
C	0.0001
Fe	0.0008
Si	0.0002

[a]Composition based on information provided by Brush Wellman. Heat number 5226, Beryllium assay 99.4%

Table 3.4. Be window transmission

Line	Energy (keV)	Transmission
^{55}Fe Kα	5.89	0.9363(6)
^{55}Fe Kβ	6.49	0.9485(16)
Cu Kα	8.05	0.9685(7)
Zn Kα	8.64	0.9652(21)
Cu Kβ	8.91	0.9759(7)
Ge Kα	9.88	0.9805(7)
Ge Kβ	10.98	0.9834(18)
Ag Kα	22.16	0.9967(11)
Cd Kα	23.17	0.9941(9)

We undertook the following measurements for 3 Be windows: first, we measured the full attenuation curve at the center of the window with I/I_0 measurements. Next, we move the window and measure the attenuation at a single energy at various positions on the window. The attenuation for each of the three windows is in excellent agreement with expectations. The window thickness varies slightly with radius (within manufacturing specifications). On examining the results, the more uniform windows were selected as flight windows. These windows are nominally 110 μm thick and one of them shows a slight radial increase in attenuation (Figure 3.16).

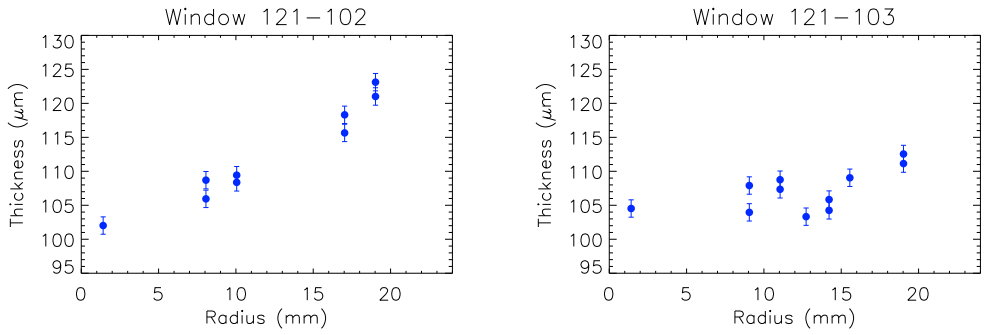

Figure 3.16. Radial variation of thickness for flight Be windows. The thickness was calculated using the 5.89 keV ^{55}Fe Kα and 6.49 keV ^{55}Fe Kβ lines.

3.7.2 Optics Cover

Thermal covers for optics are made of Mylar film. Ribs added for structural integrity occupy about 1% of the area of the cover. Calibration requirements for these covers are folded into requirements for overall optics calibrations. We were tasked with verifying the transparency of these covers at low energies. We selected the ^{55}Fe source and the Amptex Si detector for calibration. The source radiates a rather wide X-ray beam, while the detector has a 2.38 mm circular collimator. As in the Be window calibrations, we first lined up the source and detector and measured the source flux I_0. We mounted a "flight spare" optics cover close to the detector and measured the attenuation for at various points on the surface (Figure 3.17). The mean transparency at 5.9 keV is 96%, in exact agreement with design requirements.

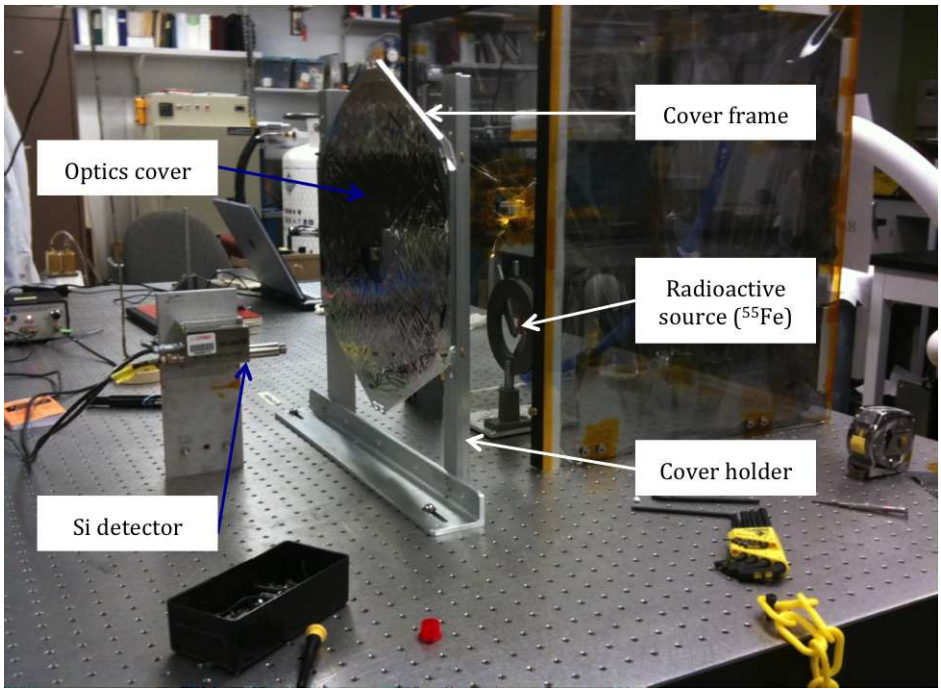

Figure 3.17. Setup used for measuring the transparency of the optics thermal cover at low (∼6 keV) energies.

3.8 Summary

As I write this thesis, all the calibrated components have been mounted in the Focal Plane Modules, and the instrument and spacecraft are ready for launch. Calibration data has been processed into data products required for analyzing astrophysical source data from NuSTAR. The results are being converted into the appropriate format for distribution with NuSTARDAS. With NuSTAR scheduled for launch in Summer 2012, we look forward to the exciting science to come!

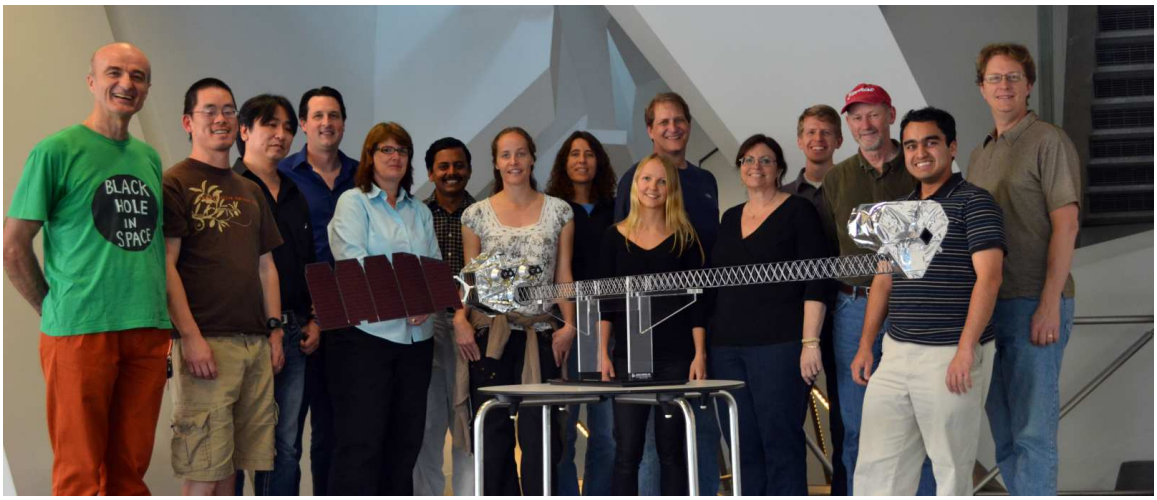

Part Two: Masses of Neutron Stars

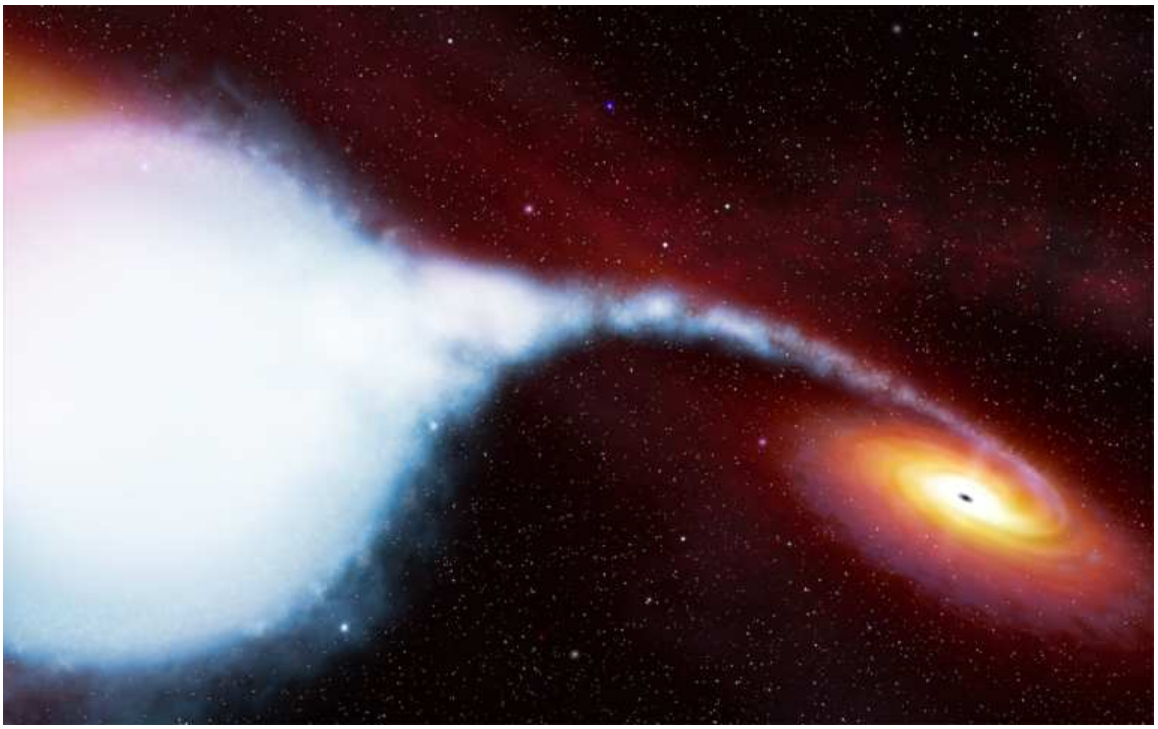

X-Mas: A Search for eXtra Massive Neutron Stars

Image: Artists illustration of a galactic Black Hole High-Mass X-ray Binary Cygnus X-1.

Credit: ESA/Hubble, via Wikimedia Commons.

Neutron Stars

This is an abridged version of the thesis for file size considerations. Please download the complete version from http://thesis.library.caltech.edu.

Appendix

This is an abridged version of the thesis for file size considerations. Please download the complete version from http://thesis.library.caltech.edu.

Bibliography

Abdo, A. A., Ackermann, M., Ajello, M., Atwood, W. B., Axelsson, M., et al. 2010, The Astrophysical Journal Supplement Series, 187, 460

Agrawal, P. 2006, Advances in Space Research, 38, 2989

Alpar, M. A., Cheng, A. F., Ruderman, M. A., & Shaham, J. 1982, Nature, 300, 728

Arzoumanian, Z., Cordes, J. M., & Wasserman, I. 1999, The Astrophysical Journal, 520, 696

Bailes, M., Bates, S. D., Bhalerao, V., Bhat, N. D. R., Burgay, M., et al. 2011, Science, 1

Barthelmy, S. D., Barbier, L. M., Cummings, J. R., Fenimore, E. E., Gehrels, N., et al. 2005, Space Science Reviews, 120, 143

Barziv, O., Kaper, L., Van Kerkwijk, M. H., Telting, J. H., & Van Paradijs, J. 2001, Astronomy and Astrophysics, 377, 925

Bessell, M. S., Castelli, F., & Plez, B. 1998, Astronomy and Astrophysics, 250, 231

Bhalerao, V. B., & Kulkarni, S. R. 2011, The Astrophysical Journal, 737, L1

Bhalerao, V. B., van Kerkwijk, M. H., Harrison, F. A., Kasliwal, M. M., Kulkarni, S. R., & Rana, V. R. 2010, The Astrophysical Journal, 721, 412

Bhattacharya, D., & van den Heuvel, E. P. J. 1991, Physics Reports, 203, 1

Bildsten, L. 1998, The Astrophysical Journal, 501, L89

—. 2003, Radio Pulsars, 302

Blackburn, J. K. 1995, Astronomical Data Analysis Software and Systems IV, 77

Bolotnikov, A., Cook, W., Harrison, F., Wong, A.-S., Schindler, S., & Eichelberger, A. 1999, Nuclear Instruments and Methods in Physics Research Section A: Accelerators, Spectrometers, Detectors and Associated Equipment, 432, 326

Bonnet-Bidaud, J. M., & Mouchet, M. 1998, Astronomy and Astrophysics, 12, 9

Bonsema, P. F. J., & van den Heuvel, E. P. J. 1985, Astronomy and Astrophysics, 146

Brott, I., de Mink, S. E., Cantiello, M., Langer, N., de Koter, A., et al. 2011, Astronomy & Astrophysics, 530, A115

Camero Arranz, A., Wilson, C. A., Finger, M. H., & Reglero, V. 2007, Astronomy and Astrophysics, 473, 551

Camilo, F., Thorsett, S. E., & Kulkarni, S. R. 1994, The Astrophysical Journal, 421, L15

Casares, J., Hernández, J. I. G., Israelian, G., & Rebolo, R. 2010, Monthly Notices of the Royal Astronomical Society, 401, 2517

Cenko, S. B., Fox, D. B., Moon, D., Harrison, F. A., Kulkarni, S. R., et al. 2006, Publications of the Astronomical Society of the Pacific, 118, 1396

Chabrier, G., Brassard, P., Fontaine, G., & Saumon, D. 2000, The Astrophysical Journal, 543, 216

Chaty, S. 2011, Evolution of compact binaries. Proceedings of a workshop held at Hotel San Martín, 447

Chaty, S., Zurita Heras, J. A., & Bodaghee, A. 2010, eprint arXiv:1012.2318

Christensen, F. E., Hornstrup, A., Westergaard, N. J., Schnopper, H. W., Wood, J., & Parker, K. 1992, In: Multilayer and grazing incidence X-ray/EUV optics; Proceedings of the Meeting, 160

Christensen, F. E., Jakobsen, A. C., Brejnholt, N. F., Madsen, K. K., Hornstrup, A., et al. 2011, in Society of Photo-Optical Instrumentation Engineers (SPIE) Conference Series, Vol. 8147, 81470U–81470U–19

Clark, D. J., Hill, A. B., Bird, A. J., McBride, V. A., Scaringi, S., & Dean, A. J. 2009, Monthly Notices of the Royal Astronomical Society: Letters, 399, L113

Clark, J. S., Goodwin, S. P., Crowther, P. A., Kaper, L., Fairbairn, M., Langer, N., & Brocksopp, C. 2002, Astronomy and Astrophysics, 392, 909

Cordes, J. M., & Lazio, T. J. W. 2002, eprint arXiv:astro-ph/0207156

Cox, A. N. 2000, Allen's astrophysical quantities

Cropper, M. 1990, Space Science Reviews, 54, 195

de Vaucouleurs, G., de Vaucouleurs, A., Corwin, Herold G., J., Buta, R. J., Paturel, G., & Fouque, P. 1991, Volume 1-3, 1

Deloye, C. J., & Bildsten, L. 2003, The Astrophysical Journal, 598, 1217

Demorest, P. B., Pennucci, T., Ransom, S. M., Roberts, M. S. E., & Hessels, J. W. T. 2010, Nature, 467, 1081

Denisenko, D. V., Kryachko, T. V., & Satovskiy, B. L. 2009, The Astronomer's Telegram

Drave, S. P., Bird, A. J., Townsend, L. J., Hill, A. B., McBride, V. A., Sguera, V., Bazzano, A., & Clark, D. J. 2012, Astronomy & Astrophysics, 539, A21

Edwards, R., Bailes, M., van Straten, W., & Britton, M. 2001, Monthly Notices of the Royal Astronomical Society, 326, 358

Eggleton, P. P. 1983, The Astrophysical Journal, 268, 368

Figueira, P., Pepe, F., Lovis, C., & Mayor, M. 2010, Astronomy and Astrophysics, 515, A106

Frank, J., King, A. R., & Raine, D. J. 1985, Accretion power in astrophysics

Freedman, W. L., Madore, B. F., Gibson, B. K., Ferrarese, L., Kelson, D. D., et al. 2001, The Astrophysical Journal, 553, 47

Freire, P. C. C., Ransom, S. M., Bégin, S., Stairs, I. H., Hessels, J. W. T., Frey, L. H., & Camilo, F. 2008, The Astrophysical Journal, 675, 670

Fruchter, A. S., Stinebring, D. R., & Taylor, J. H. 1988, Nature, 333, 237

Galloway, D. K., Chakrabarty, D., Morgan, E. H., & Remillard, R. A. 2002, The Astrophysical Journal, 576, L137

Gehrels, N., Chincarini, G., Giommi, P., Mason, K. O., Nousek, J. A., et al. 2004, The Astrophysical Journal, 611, 1005

Giacconi, R., Gursky, H., Paolini, F., & Rossi, B. 1962, Physical Review Letters, 9, 439

Giacconi, R., Branduardi, G., Briel, U., Epstein, A., Fabricant, D., et al. 1979, The Astrophysical Journal, 230, 540

Gray, D. F. 2005, The Observation and Analysis of Stellar Photospheres

Grindlay, J. E., & Bailyn, C. D. 1988, Nature, 336, 48

Hailey, C. J., An, H., Blaedel, K. L., Brejnholt, N. F., Christensen, F. E., et al. 2010, in Space Telescopes and Instrumentation 2010: Ultraviolet to Gamma Ray. Edited by Arnaud, Vol. 7732, 77320T–77320T–13

Hansen, B. M. S., Shih, H.-Y., & Currie, T. 2009, The Astrophysical Journal, 691, 382

Harrison, F. A., Christensen, F. E., Craig, W., Hailey, C., Baumgartner, W., et al. 2006, Experimental Astronomy, 20, 131

Harrison, F. A., Boggs, S., Christensen, F., Craig, W., Hailey, C., et al. 2010, in Space Telescopes and Instrumentation 2010: Ultraviolet to Gamma Ray. Edited by Arnaud, Vol. 7732, 77320S–77320S–8

Harrison, M., McGregor, D., & Doty, F. 2008, Physical Review B, 77

Harwit, M. 2003, Physics Today, 56, 38

Hellier, C. 2001, Cataclysmic Variable Stars

—. 2002, The Physics of Cataclysmic Variables and Related Objects, 261

Hessels, J., Ransom, S., Roberts, M., Kaspi, V., Livingstone, M., Tam, C., & Crawford, F. 2005, Binary Radio Pulsars, 328

Hessels, J. W. T., Ransom, S. M., Stairs, I. H., Freire, P. C. C., Kaspi, V. M., & Camilo, F. 2006, Science (New York, N.Y.), 311, 1901

Hilditch, R. W. 2001, An Introduction to Close Binary Stars, 1st edn. (Cambridge, UK: Cambridge University Press)

Hilditch, R. W., Howarth, I. D., & Harries, T. J. 2005, Monthly Notices of the Royal Astronomical Society, 357, 304

Hulleman, F., in 't Zand, J. J. M., & Heise, J. 1998, Astronomy and Astrophysics, 337, L25

in 't Zand, J. J. M. 2005, Astronomy and Astrophysics, 441, L1

Iniewski, K. 2010, Semiconductor radiation detection systems (Boca Raton FL: CRC Press/Taylor & Francis)

Jacoby, B. A., Hotan, A., Bailes, M., Ord, S., & Kulkarni, S. R. 2005, The Astrophysical Journal, 629, L113

Jahoda, K., Swank, J. H., Giles, A. B., Stark, M. J., Strohmayer, T., Zhang, W., & Morgan, E. H. 1996, Proc. SPIE Vol. 2808, 2808, 59

Jester, S., Schneider, D. P., Richards, G. T., Green, R. F., Schmidt, M., et al. 2005, The Astronomical Journal, 130, 873

Joss, P. C., & Rappaport, S. A. 1984, Annual Review of Astronomy and Astrophysics, 22, 537

Juett, A. M., Psaltis, D., & Chakrabarty, D. 2001, The Astrophysical Journal, 560, L59

Kaspi, V. M., Lyne, A. G., Manchester, R. N., Crawford, F., Camilo, F., et al. 2000, The Astrophysical Journal, 543, 321

Kaur, R., Wijnands, R., Paul, B., Patruno, A., & Degenaar, N. 2010, Monthly Notices of the Royal Astronomical Society, 402, 2388

Keith, M. J., Jameson, A., Van Straten, W., Bailes, M., Johnston, S., et al. 2010, Monthly Notices of the Royal Astronomical Society, 409, 619

Keith, M. J., Johnston, S., Ray, P. S., Ferrara, E. C., Saz Parkinson, P. M., et al. 2011, Monthly Notices of the Royal Astronomical Society, 414, 1292

Kiziltan, B., Kottas, A., & Thorsett, S. E. 2010, eprint arXiv:1011.4291

Kiziltan, B., & Thorsett, S. E. 2010, The Astrophysical Journal, 715, 335

Knigge, C., Coe, M. J., & Podsiadlowski, P. 2011, Nature, 479, 372

Kolb, U., King, A. R., & Baraffe, I. 2001, Monthly Notices of the Royal Astronomical Society, 321, 544

Kzlolu, U., Kzlolu, N., Baykal, A., Yerli, S. K., & Özbey, M. 2007, Astronomy and Astrophysics, 470, 1023

Lai, D., Abrahams, A. M., & Shapiro, S. L. 1991, The Astrophysical Journal, 377, 612

Landsman, W. B. 1993, Astronomical Data Analysis Software and Systems II, 52

Lang, D., Hogg, D. W., Mierle, K., Blanton, M., & Roweis, S. 2010, The Astronomical Journal, 139, 1782

Lattimer, J., & Prakash, M. 2005, Physical Review Letters, 94

Lattimer, J. M., & Prakash, M. 2004, Science (New York, N.Y.), 304, 536

—. 2007, Physics Reports, 442, 109

Lattimer, J. M., Prakash, M., Day, R. R., & Year, M. 2010, eprint arXiv:1012.3208, 1

Law, N. M., Kulkarni, S. R., Dekany, R. G., Ofek, E. O., Quimby, R. M., et al. 2009, Publications of the Astronomical Society of the Pacific, 121, 1395

Lebrun, F., Leray, J. P., Lavocat, P., Crtolle, J., Arqus, M., et al. 2003, Astronomy and Astrophysics, 411, L141

Lin, J., Rappaport, S., Podsiadlowski, P., Nelson, L., Paxton, B., & Todorov, P. 2011, The Astrophysical Journal, 732, 70

Liu, Q. Z., van Paradijs, J., & van den Heuvel, E. P. J. 2005, Astronomy and Astrophysics, 442, 1135

—. 2006, Astronomy and Astrophysics, 455, 1165

Longair, M. S. 1992, High Energy Astrophysics

Madsen, K. K., Harrison, F. a., Mao, P. H., Christensen, F. E., Jensen, C. P., Brejnholt, N., Koglin, J., & Pivovaroff, M. J. 2009, Proceedings of SPIE, 7437, 743716

Manchester, R. N., Hobbs, G. B., Teoh, A., & Hobbs, M. 2005, The Astronomical Journal, 129, 1993

Mao, P. H., Harrison, F. A., Windt, D. L., & Christensen, F. E. 1999, Applied Optics, 38, 4766

Markwardt, C. B. 2009, Astronomical Data Analysis Software and Systems XVIII ASP Conference Series, 411

Mason, A. B., Clark, J. S., Norton, A. J., Crowther, P. A., Tauris, T. M., Langer, N., Negueruela, I., & Roche, P. 2011a, Monthly Notices of the Royal Astronomical Society, 000, 10

Mason, A. B., Norton, A. J., Clark, J. S., Negueruela, I., & Roche, P. 2011b, Astronomy & Astrophysics, 532, A124

Mason, A. B., Norton, A. J., Clark, J. S., Roche, P., & Negueruela, I. 2010, Société Royale des Sciences de Liège, 80, 699

Massey, P., Morrell, N. I., Neugent, K. F., Penny, L. R., Eastwood, K.-D., & Gies, D. R. 2012, Physics

McCarthy, J. K., Cohen, J. G., Butcher, B., Cromer, J., Croner, E., et al. 1998, Proc. SPIE Vol. 3355, 3355, 81

McConnachie, A. W., Irwin, M. J., Ferguson, A. M. N., Ibata, R. A., Lewis, G. F., & Tanvir, N. 2005, Monthly Notices of the Royal Astronomical Society, 356, 979

McLean, I. S., McGovern, M. R., Burgasser, A. J., Kirkpatrick, J. D., Prato, L., & Kim, S. S. 2003, The Astrophysical Journal, 596, 561

McLean, I. S., Becklin, E. E., Bendiksen, O., Brims, G., Canfield, J., et al. 1998, Proc. SPIE Vol. 3354, 3354, 566

Mighell, K. J. 1999, Astronomical Data Analysis Software and Systems VIII, 172

Munari, U., Sordo, R., Castelli, F., & Zwitter, T. 2005, Astronomy and Astrophysics, 442, 1127

MunozDarias, T., Casares, J., & MartinezPais, I. G. 2005, The Astrophysical Journal, 635, 502

Negueruela, I., & Schurch, M. P. E. 2007, Astronomy and Astrophysics, 461, 631

Niemela, A., & Sipila, H. 1994, IEEE Transactions on Nuclear Science, 41, 1054

Nomoto, K. 1984, The Astrophysical Journal, 277, 791

Oke, J. B., & Gunn, J. E. 1982, Publications of the Astronomical Society of the Pacific, 94, 586

Oke, J. B., Cohen, J. G., Carr, M., Cromer, J., Dingizian, A., et al. 1995, Publications of the Astronomical Society of the Pacific, 107, 375

Özel, F., Psaltis, D., Narayan, R., & McClintock, J. E. 2010, The Astrophysical Journal, 725, 1918

Özel, F., Psaltis, D., Narayan, R., & Villarreal, A. S. 2012, arXiv eprint

Paczynski, B. 1971, Annual Review of Astronomy and Astrophysics, 9, 183

Paul, B., & Naik, S. 2011, Bulletin of the Astronomical Society of India, 39, 429

Pellizza, L. J., Chaty, S., & Negueruela, I. 2006, Astronomy and Astrophysics, 455, 653

Pietsch, W., Misanovic, Z., Haberl, F., Hatzidimitriou, D., Ehle, M., & Trinchieri, G. 2004, Astronomy and Astrophysics, 426, 11

Pietsch, W., Plucinsky, P. P., Haberl, F., Shporer, A., & Mazeh, T. 2006, The Astronomer's Telegram, 905, 1

Pietsch, W., Haberl, F., Gaetz, T. J., Hartman, J. D., Plucinsky, P. P., et al. 2009, The Astrophysical Journal, 694, 449

Podsiadlowski, P. 1993, in Planets around pulsars; Proceedings of the Conference, ed. J. A. Phillips, S. E. Thorsett, & S. R. Kulkarni, Vol. 36, 149–165

Poole, T. S., Breeveld, A. A., Page, M. J., Landsman, W., Holland, S. T., et al. 2007, Monthly Notices of the Royal Astronomical Society, 383, 627

Quaintrell, H., Norton, A. J., Ash, T. D. C., Roche, P., Willems, B., Bedding, T. R., Baldry, I. K., & Fender, R. P. 2003, Astronomy and Astrophysics, 401, 313

Radhakrishnan, V., & Srinivasan, G. 1982, Current Science, 51, 1096

Rahoui, F., Chaty, S., Lagage, P.-O., & Pantin, E. 2008, Astronomy and Astrophysics, 484, 801

Ramsay, G., Cropper, M., Wu, K., Mason, K. O., Córdova, F. A., & Priedhorsky, W. 2004, Monthly Notices of the Royal Astronomical Society, 350, 1373

Rappaport, S., Podsiadlowski, P., Joss, P. C., Di Stefano, R., & Han, Z. 1995, Monthly Notices of the Royal Astronomical Society, 273, 731

Rappaport, S. A., & Joss, P. C. 1983, IN: Accretion-driven stellar X-ray sources (A84-35577 16-90). Cambridge and New York, 1

Rasio, F. A., Shapiro, S. L., & Teukolsky, S. A. 1992, Astronomy and Astrophysics (ISSN 0004-6361), 256

Reig, P. 2011, Astrophysics and Space Science, 332, 1

Reig, P., Negueruela, I., Fabregat, J., Chato, R., Blay, P., & Mavromatakis, F. 2004, Astronomy and Astrophysics, 421, 673

Remillard, R. A., & McClintock, J. E. 2006, Annual Review of Astronomy and Astrophysics, 44, 49

Rephaeli, Y., Nevalainen, J., Ohashi, T., & Bykov, A. M. 2008, Space Science Reviews, 134, 71

Roberts, M. S. E., Gotthelf, E. V., Halpern, J. P., Brogan, C. L., & Ransom, S. M. 2007, Proceedings of the 363. WE-Heraeus Seminar on Neutron Stars and Pulsars 40 years after the discovery. Edited by W. Becker and H. H. Huang. MPE-Report 291. ISSN 0178-0719. Published by the Max Planck Institut für extraterrestrische Physik

Rockosi, C., Stover, R., Kibrick, R., Lockwood, C., Peck, M., et al. 2010, in Ground-based and Airborne Instrumentation for Astronomy III. Edited by McLean, Vol. 7735, 77350R–77350R–11

Schlegel, D. J., Finkbeiner, D. P., & Davis, M. 1998, The Astrophysical Journal, 500, 525

Schwab, J., Podsiadlowski, P., & Rappaport, S. 2010, The Astrophysical Journal, 719, 722

Shevchuk, A. S., Fox, D. B., Turner, M., & Rutledge, R. E. 2009, The Astronomer's Telegram

Shklovskii, I. S. 1970, Soviet Astronomy, 13

Shporer, A., Hartman, J., Mazeh, T., & Pietsch, W. 2006, The Astronomer's Telegram, 913, 1

Sidoli, L. 2011, Advances in Space Research, 48, 88

Simcoe, R. A., Metzger, M. R., Small, T. A., & Araya, G. 2000, American Astronomical Society, 32

Smith, D. M. 2004, The Astronomer's Telegram

Stappers, B. W., Bailes, M., Manchester, R. N., Sandhu, J. S., & Toscano, M. 1998, The Astrophysical Journal, 499, L183

Stappers, B. W., van Kerkwijk, M. H., Lane, B., & Kulkarni, S. R. 1999, The Astrophysical Journal, 510, L45

Steidel, C. C., Shapley, A. E., Pettini, M., Adelberger, K. L., Erb, D. K., Reddy, N. A., & Hunt, M. P. 2004, The Astrophysical Journal, 604, 534

Steiner, A. W., Lattimer, J. M., & Brown, E. F. 2010, The Astrophysical Journal, 722, 33

Sunyaev, R. A., Grebenev, S. A., Lutovinov, A. A., Rodriguez, J., Mereghetti, S., Gotz, D., & Courvoisier, T. 2003, The Astronomer's Telegram, 190, 1

Takahashi, T., Abe, K., Endo, M., Endo, Y., Ezoe, Y., et al. 2007, Publications of the Astronomical Society of Japan

Tauris, T. M., Langer, N., & Kramer, M. 2011, Monthly Notices of the Royal Astronomical Society, 416, 2130

Timmes, F. X., Woosley, S. E., & Weaver, T. A. 1996, The Astrophysical Journal, 457, 834

Torres, G. 2010, The Astronomical Journal, 140, 1158

Toscano, M., Sandhu, J. S., Bailes, M., Manchester, R. N., Britton, M. C., Kulkarni, S. R., Anderson, S. B., & Stappers, B. W. 1999, Monthly Notices of the Royal Astronomical Society, 307, 925

Tousey, R., Watanabe, K., & Purcell, J. 1951, Physical Review, 83, 792

Ubertini, P., Lebrun, F., Di Cocco, G., Bazzano, A., Bird, A. J., et al. 2003, Astronomy and Astrophysics, 411, L131

Valentim, R., Rangel, E., & Horvath, J. E. 2011, Monthly Notices of the Royal Astronomical Society, 414, 1427

van den Heuvel, E. P. J., & Bonsdema, P. T. J. 1984, Astronomy and Astrophysics (ISSN 0004-6361), 139

van der Meer, A., Kaper, L., van Kerkwijk, M. H., Heemskerk, M. H. M., & van den Heuvel, E. P. J. 2007, Astronomy and Astrophysics, 473, 523

van Dokkum, P. G. 2001, Publications of the Astronomical Society of the Pacific, 113, 1420

van Kerkwijk, M. H., Breton, R. P., & Kulkarni, S. R. 2011, The Astrophysical Journal, 728, 95

van Kerkwijk, M. H., van Paradijs, J., Zuiderwijk, E. J., Hammerschlag-Hensberge, G., Kaper, L., & Sterken, C. 1995, Astronomy and Astrophysics

Verbiest, J. P. W., Bailes, M., van Straten, W., Hobbs, G. B., Edwards, R. T., et al. 2008, The Astrophysical Journal, 679, 675

Voges, W., Aschenbach, B., Boller, T., Bräuninger, H., Briel, U., et al. 1999, Astronomy and Astrophysics

Walborn, N. R., & Fitzpatrick, E. L. 1990, Publications of the Astronomical Society of the Pacific, 102, 379

Warner, B. 1995, Camb. Astrophys. Ser., 28

Weisskopf, M. C., Tananbaum, H. D., Van Speybroeck, L. P., & O'Dell, S. L. 2000, Proc. SPIE Vol. 4012, 4012, 2

Wijers, R. A. M. J., van den Heuvel, E. P. J., van Kerkwijk, M. H., & Bhattacharya, D. 1992, Nature, 355, 593

Wilson, C. A., Finger, M. H., Harmon, B. A., Chakrabarty, D., & Strohmayer, T. 1998, The Astrophysical Journal, 499, 820

Wilson, C. A., Weisskopf, M. C., Finger, M. H., Coe, M. J., Greiner, J., Reig, P., & Papamastorakis, G. 2005, The Astrophysical Journal, 622, 1024

Wolszczan, A., & Frail, D. A. 1992, Nature, 355, 145

Wolter, H. 1952a, Annalen der Physik, 445, 286

—. 1952b, Annalen der Physik, 445, 94

York, D. G., Adelman, J., Anderson, J., Anderson, S. F., Annis, J., et al. 2000, The Astronomical Journal, 120, 1579

Zhang, C. M., Wang, J., Zhao, Y. H., Yin, H. X., Song, L. M., et al. 2011, Astronomy & Astrophysics, 527, A83

Zwitter, T., Castelli, F., & Munari, U. 2004, Astronomy and Astrophysics, 417, 1055